ELEMENTA
Science of the Anthropocene

Estapa, M, et al. 2021. Biogenic sinking particle fluxes and sediment trap collection efficiency at Ocean Station Papa. *Elem Sci Anth*, 9: 1. DOI: https://doi.org/10.1525/elementa.2020.00122

RESEARCH ARTICLE

Biogenic sinking particle fluxes and sediment trap collection efficiency at Ocean Station Papa

Margaret Estapa[1,2,*], Ken Buesseler[3], Colleen A. Durkin[4], Melissa Omand[5], Claudia R. Benitez-Nelson[6], Montserrat Roca-Martí[3], Elly Breves[2,7], R. P. Kelly[5], and Steve Pike[3]

Comprehensive field observations characterizing the biological carbon pump (BCP) provide the foundation needed to constrain mechanistic models of downward particulate organic carbon (POC) flux in the ocean. Sediment traps were deployed three times during the EXport Processes in the Ocean from RemoTe Sensing campaign at Ocean Station Papa in August–September 2018. We propose a new method to correct sediment trap sample contamination by zooplankton "swimmers." We consider the advantages of polyacrylamide gel collectors to constrain swimmer influence and estimate the magnitude of possible trap biases. Measured sediment trap fluxes of thorium-234 are compared to water column measurements to assess trap performance and estimate the possible magnitude of fluxes by vertically migrating zooplankton that bypassed traps. We found generally low fluxes of sinking POC (1.38 $\pm$ 0.77 mmol C m^{-2} d^{-1} at 100 m, n = 9) that included high and variable contributions by rare, large particles. Sinking particle sizes generally decreased between 100 and 335 m. Measured ^{234}Th fluxes were smaller than water column ^{234}Th fluxes by a factor of approximately 3. Much of this difference was consistent with trap undersampling of both small (<32 μm) and rare, large particles (>1 mm) and with zooplankton active migrant fluxes. The fraction of net primary production exported below the euphotic zone (0.1% light level; Ez-ratio = 0.10 $\pm$ 0.06; ratio uncertainties are propagated from measurements with n = 7–9) was consistent with prior, late summer studies at Station P, as was the fraction of material exported to 100 m below the base of the euphotic zone (T_{100}, 0.55 $\pm$ 0.35). While both the Ez-ratio and T_{100} parameters varied weekly, their product, which we interpret as overall BCP efficiency, was remarkably stable (0.055 $\pm$ 0.010), suggesting a tight coupling between production and recycling at Station P.

Keywords: Biological carbon pump, Ocean Station Papa, Sediment traps, Carbon flux, Particle size distribution, Swimmers

1. Introduction

The downward transport of particulate organic matter in the ocean plays a critical role in the long-term sequestration of carbon dioxide and contaminants as well as serving as a food source for benthic foodwebs (McKinley et al., 2017). These biologically mediated mechanisms of organic matter transfer, collectively known as the "biological carbon pump" (BCP), vary in space and time. Their relative importance depends upon the structure of the ecosystem as influenced by chemical and physical ocean properties. Observations that sufficiently resolve the dynamic processes that comprise the BCP are challenging to make, which limits our ability to predict how BCP efficiency changes as ocean properties shift.

The transfer of carbon to depth via gravitationally sinking particles is generally thought to be the single largest flux pathway in most marine settings (Boyd et al., 2019). Carbon can also be exported from the surface ocean by vertically migrating organisms that feed at the surface and transfer carbon to depth and by physical mixing or subduction of suspended particulate organic carbon (POC) and dissolved organic carbon (DOC) from enriched surface

[1] School of Marine Sciences, Darling Marine Center, University of Maine, Walpole, ME, USA
[2] Department of Geosciences, Skidmore College, Saratoga Springs, NY, USA
[3] Department of Marine Chemistry & Geochemistry, Woods Hole Oceanographic Institution, Woods Hole, MA, USA
[4] Moss Landing Marine Laboratories, San Jose State University, Moss Landing, CA, USA
[5] Graduate School of Oceanography, University of Rhode Island, Narragansett, RI, USA
[6] School of the Earth, Ocean and Environment, University of South Carolina, Columbia, SC, USA
[7] Rensselaer Astrobiology Research and Education Center, Rensselaer Polytechnic Institute, Troy, NY, USA
* Corresponding author:
Email: margaret.estapa@maine.edu

waters into deeper depths (Levy et al., 2013; Steinberg and Landry, 2017). The fraction of exported carbon that is sequestered over long timescales is dependent on the depth penetration below the winter mixed layer (Palevsky and Doney, 2018). Slowly sinking particles and nonsinking POC and labile DOC are thought to be remineralized near the surface and returned to the atmosphere, while carbon delivered by more rapidly sinking particles and by vertical migrators is retained in the ocean interior over millennial to longer timescales (Boyd et al., 2019).

The traditional tool used to measure sinking fluxes of particles in the upper mesopelagic zone is the drifting sediment trap (Gardner, 1977; Buesseler et al., 2007). Buesseler et al. (2007) reviewed the advantages, disadvantages, and designs of upper ocean sediment traps comprehensively; we summarize a few relevant points here. Among sediment trap advantages are their unequivocal separation of sinking from suspended material, their return of samples for detailed laboratory analyses, and their relatively well-constrained sampling periods. Among their disadvantages are potential hydrodynamic sorting effects, their short collection timescale, their inability to measure fluxes of carbon actively transported by vertical migrators, and their susceptibility to contamination by zooplankton "swimmers" that enter traps during collection (Buesseler et al., 2007). These considerations, as well as the diversity of sampling objectives in BCP research programs, have led to an assortment of trap designs currently in use (Buesseler et al., 2007; Baker et al., 2020). These include different collector shapes (cylindrical and conical), trap lids, sample preservatives, and supporting platforms (moored or drifting arrays and neutral floats).

Here, we describe a series of sediment trap deployments conducted as part of the EXport Processes in the Ocean from RemoTe Sensing (EXPORTS) program in the vicinity of Ocean Station Papa (Station P; 50°N, 145°W) in August and September 2018 (Siegel et al., n.d.). The goal of the EXPORTS program is to characterize comprehensively all of the component processes of the BCP, while simultaneously collecting a full suite of inherent and apparent optical properties that together can be used to develop predictive models of BCP fluxes driven by ocean color remote sensing observations (Siegel et al., 2016). The trap sampling plan was designed to provide information on the biological and chemical character of the sinking particles, their size distributions, and how their fluxes vary in time. To achieve these goals, we utilized multiple, complementary methods including different trap designs (Baker et al., 2020), simultaneous bulk sample collection and gel collectors (Durkin et al., 2021), and time-resolved, 3D sampling of thorium-234 activities (Buesseler et al., 2020a). This combination of methods also allowed us to examine potential biases in each measurement. Here, we describe the deployments and their results and contextualize them relative to other observational components of the EXPORTS study. We also discuss the trap fluxes in the context of historical observations from Station P.

2. Methods

2.1. Deployment design

The EXPORTS study design (described in detail in Siegel et al., n.d.) consisted of a suite of measurement tools operating in different spatiotemporal sampling modes. Autonomous platforms provided continuity with the time periods preceding and following ship occupations in August–September 2018. Spatially distributed hydrographic, chemical, and optical measurements were made from the R/V *Sally Ride*, while longer term measurements, including sediment trap deployments, were made in a water-following frame of reference from the R/V *Roger Revelle*, which tracked a Lagrangian float deployed at a drift depth of 100 $\pm$ 10 m (Siegel et al., n.d.). All measurements were conducted in repeated, 8-day cycles, referred to as "epochs." During the cruise, the depth of the euphotic zone (defined as the 0.1% light level with respect to the surface) was determined from a series of radiometer profiles (Compact Optical Profiling System, Biospherical) conducted from the *Revelle*. The deployment and analysis details are described by Siegel et al. (n.d.). Sediment traps were deployed once per epoch for 3–6 days. Deployment locations, times, and depths are summarized in **Figure 1** and **Table 1**.

Two sediment trap designs were utilized in the study. A drifting, five-depth, surface-tethered trap (STT) array collected sinking particles at 95, 145, 195, 330, and 500 m in Epoch 1. A repair of the STT array after weather damage during Epoch 1 increased all STT trap depths by 10 m in Epochs 2 and 3. Six neutrally buoyant sediment traps (NBSTs; Estapa et al., 2020) were also deployed alongside the STT array. Two NBSTs were deployed at 95 m and 195 m, and one each at 145 m and 330 m. **Figure 1** shows trajectories of the NBSTs at different depths in each epoch. A handful of NBST deployment irregularities occurred in Epochs 2 and 3 and are described in detail by Estapa et al. (2020). For example, in Epoch 2, NBST-304 (targeted at 195 m) had its initial depressor weight become entangled during deployment. The trap, therefore, did not immediately resurface, although trap lids closed on schedule. NBST-304 resurfaced later, partway through Epoch 3. In Epoch 3, NBST-302 and NBST-303 (targeted at 195 and 145 m, respectively) resurfaced on time, but due to a communication problem, repeated their dive cycle a second time (with trap lids closed) prior to recovery.

Regardless of SST versus NBST platform, four trap tubes of the "CLAP" design (Lamborg et al., 2008) were deployed at each trap depth and consisted of a polycarbonate tube with a collection area of 0.0113 m^2, and a lid attached with an elastic bungee. Lids were deployed open, then were released from a timed burnwire to snap closed at the end of the planned deployment period. On each platform, two tubes carried 500 mL of 70 ppt salinity, 0.1% formaldehyde-poisoned brine buffered with borate to pH 8.5 that was overlain by 1-μm filtered surface seawater. A third tube carried homemade RNAlater (Malmstrom, 2015) overlain by filtered seawater to preserve genetic material, and a fourth tube carried a polyacrylamide gel collector overlain by filtered surface seawater (Durkin et al., 2015; Durkin et al., 2021). Each NBST carried

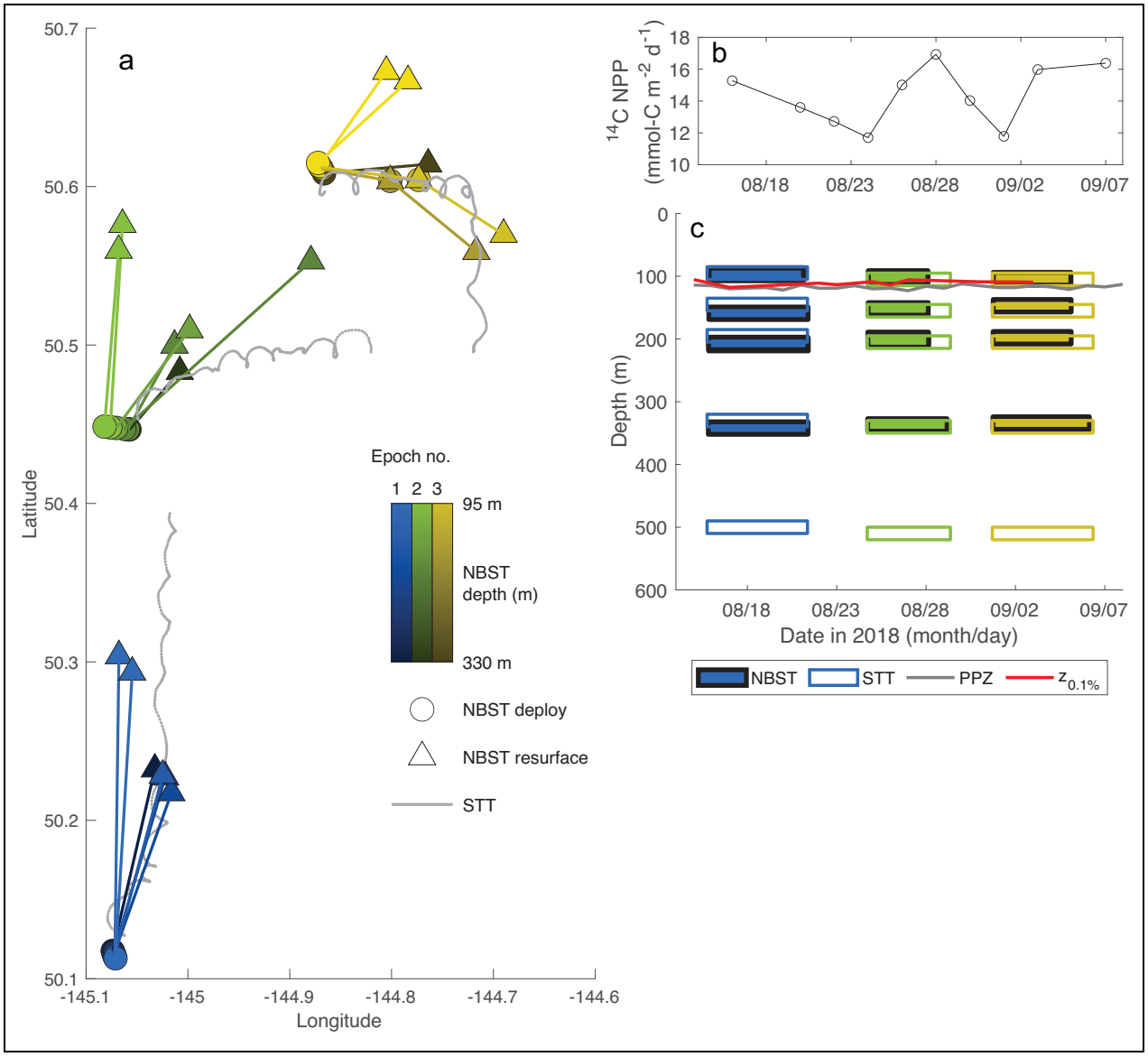

Figure 1. Deployment locations and timings. (a) Deployment (circles) and recovery locations (triangles) and drift trajectories (where known) of traps deployed during this study. Color shades for neutrally buoyant sediment traps (NBSTs) correspond to the trap drift depth. (b) Depth-integrated net primary production (NPP) measured using ^{14}C during the cruise. (c) Depths and deployment periods for NBST (filled bars) and surface-tethered traps (STT; open bars). Primary production zone (PPZ) depth (gray line) and photosynthetically available radiation (PAR) depth ($z_{0.1\%}$, red line) shown for reference. Panel a was originally published as figure 8 in Estapa et al. (2020). © American Meteorological Society (used with permission). DOI: https://doi.org/10.1525/elementa.2020.00122.f1

a transmissometer (C-Rover 2K, WET Labs Inc., Philomath, OR, USA) used as an optical sediment trap (OST; Estapa et al. 2017). At each of the upper three STT depths, the array also included a RESPIRE trap used to measure particle-attached microbial respiration rates and is discussed in detail by Santoro et al. (2020). An acoustic current meter was deployed immediately below the 500-m STT depth to measure relative water motions.

2.2. Sample analysis

2.2.1. Bulk sample processing and analysis

After recovery, each trap tube was removed from its host platform and allowed to stand in the lab for at least an hour to allow particles to finish settling to the bottom of the tube. Replicate formalin-poisoned brine tubes at each depth were combined and drained through a 335-µm polyester screen. Tubes and screens were rinsed thoroughly with filtered seawater. Then, screens were manually picked clean of recognizable zooplankton "swimmers" under 7× magnification. The remaining material on each screen, presumed to consist of passively settling material only, was recombined with the sample fraction that passed through the 335 µm screen, which was not picked. The sample was then passed through a rotary wet splitter inside a flow bench (Lamborg et al., 2008; Owens et al., 2013) and divided into eight equal fractions (A–H). Fractions A, B, and C were filtered through precombusted, 25-mm diameter, quartz microfiber filters (QMA, nominal

Table 1. Summary of sediment trap deployments.[a] DOI: https://doi.org/10.1525/elementa.2020.00122.t1

				Date/Time in 2018 (UTC)		Deployment Position		Recovery Position		
Trap Type	NBST ID	Epoch	Depth (m)	Deployed	Resurfaced	Latitude (°N)	Longitude (°E)	Latitude (°N)	Longitude (°E)	Distance[b] (km)
SOLO	20	1	96	August 15, 20:23	August 21, 03:17	50.1138	−145.0718	50.3038	−145.0678	21.1
SOLO	200	1	97	August 15, 20:37	August 21, 03:27	50.1129	−145.0712	50.2934	−145.0547	20.1
APEX	303	1	159	August 15, 20:11	August 21, 09:26	50.1146	−145.0722	50.2283	−145.0248	13.1
APEX	302	1	207	August 15, 20:00	August 21, 09:17	50.1155	−145.0727	50.2173	−145.0162	12.0
APEX	304	1	209	August 15, 19:51	August 21, 09:48	50.1163	−145.0731	50.2272	−145.0223	12.9
APEX	305	1	342	August 15, 19:31	August 21, 09:23	50.1176	−145.0739	50.2323	−145.0325	13.1
STT	—	1	95, 145, 195, 330, 500	August 15, 17:53	August 21, 08:40	50.1223	−145.0754	50.3931	−145.0172	30.4
SOLO	20	2	101	August 24, 18:20	August 28, 02:24	50.4481	−145.0763	50.5760	−145.0643	14.2
SOLO	200	2	103	August 24, 18:30	August 28, 02:25	50.4485	−145.0819	50.5597	−145.0681	12.4
APEX	303	2	152	August 24, 18:07	August 28, 02:55	50.4477	−145.0705	50.5095	−144.9984	8.6
APEX	302	2	199	August 24, 17:42	August 28, 03:21	50.4468	−145.0590	50.4998	−145.0132	6.7
APEX	304[c]	2	203	August 24, 17:55	September 1, 17:27	50.4471	−145.0624	50.5530	−144.8792	17.5[c]
APEX	305	2	337	August 24, 17:30	August 29, 04:10	50.4467	−145.0574	50.4832	−145.0080	5.4
STT	—	3	105, 155, 205, 340, 510	August 24, 16:55	August 29, 08:38	50.4538	−145.0501	50.4898	−144.8312	16.0
SOLO	20	3	104	August 31, 18:17	September 5, 02:23	50.6131	−144.8706	50.6726	−144.8052	8.1
SOLO	200	3	104	August 31, 18:25	September 5, 02:24	50.6149	−144.8722	50.6667	−144.7839	8.5
APEX	303[c]	3	147	August 31, 18:08	September 5, 02:54	50.6122	−144.8698	50.6043	−144.7733	6.9
APEX	303[c]	3	147	September 5, 03:52	September 9, 17:47	50.6043	−144.7733	50.5698	−144.6900	7.0
APEX	302[c]	3	198	August 31, 18:00	September 5, 02:53	50.6112	−144.8687	50.6036	−144.8013	4.8
APEX	302[c]	3	200	September 5, 03:57	September 9, 18:17	50.6036	−144.8013	50.5590	−144.7167	7.8
APEX	305	3	334	August 31, 17:47	September 6, 03:19	50.6083	−144.8663	50.6142	−144.7640	7.2
STT	—	3	105, 155, 205, 340, 510	August 31, 16:58	September 6, 08:17	50.5996	−144.8657	50.4910	−144.7179	16.0

SOLO = SOLO-NBST; APEX = APEX-NBST; STT = surface-tethered trap array; NBST = neutrally buoyant sediment traps; UTC = Coordinated Universal Time.

[a]Data were published originally in table 3 of Estapa et al. (2020). © American Meteorological Society (used with permission).

[b]Endpoint-to-endpoint distance. See **Figure 1** for travel paths of STT arrays.

[c]Trap completed more than one mission cycle (see text). In Epoch 3, these traps are shown on separate lines because the floats resurfaced and transmitted positions after both cycles. In all cases, trap lids closed after the first cycle.

pore size 1 μm) and analyzed for total carbon and nitrogen, particulate inorganic carbon (PIC), and ^{234}Th activity. Fractions D, E, and F were filtered through pretared, 25-mm polycarbonate membrane filters (Nuclepore, nominal pore size 1 μm), rinsed with pH 8.5-buffered Milli-Q water to remove salts, and analyzed for gravimetric mass and biogenic silica (bSi). Fractions G and H were filtered onto either precombusted glass fiber or Supor filters for additional chemical analyses that will be described elsewhere. Filters from the A–F fractions were dried on board the ship and stored dry until analysis.

Dried filters A–C were immediately mounted and counted on board the ship using low-level Risø beta detectors. At sea, a subset of filters was recounted for quality control purposes. Post cruise, the "A" filters were then unmounted and split gravimetrically into quarters, and two quarters immediately consumed for analysis of ^{210}Pb/^{210}Po (Roca-Martí et al., 2020). Filters B and C were stored for at least 6 months (approximately 7 half-lives of ^{234}Th, 24.1 days) and recounted to obtain background beta emissions. The ^{234}Th activity on sinking particles at the time of collection was calculated as the difference between the initial and final background counts (or for "A" filters, the mean of Filters B–C background counts) and corrected for decay between the time of collection and the first count (Buesseler et al., 2020a). After background activities were determined, all remaining QMA filters were unmounted and split gravimetrically into halves, thirds, or quarters. At least one subfraction of each A–C filter was analyzed for total C and N content via elemental analysis and for PIC via acidification and coulometric titration (Honjo et al., 2000). Analyses on filter subfractions were scaled to whole-filter equivalents using the masses of the filter subfractions. The amount of POC per filter was determined by the difference between total C and PIC.

Filters D–F were stored dry until analysis on shore. Filters were weighed repeatedly on a microbalance until stable weights to within ± 0.005 mg were achieved. The mass of accumulated particles on each filter was computed by difference from the filter tare weight. These filters were subsequently analyzed for bSi following alkaline digestion (1 h at 95 °C in 0.2 N NaOH followed by neutralization with 1 N HCl; similar to Nelson and Brzezinski, 1989) and spectrophotometric detection using standard methods.

For each of the analyses described above, uncertainties were computed on a platform-by-platform basis, as the standard deviation among triplicate splits. Fluxes were computed by normalizing to the trap collection period (from deployment until trap lid closure), the number of splits averaged, and the combined area of tube collection. Below, we report the means and uncertainties (usually $n = 3$) determined in this manner for each trap depth (**Table 2**; Estapa, 2019). In certain cases, only two splits were available, as noted in **Table 2** and where applicable in the text. Individual split data are available in the NASA SeaBASS repository (Estapa et al., 2020).

2.2.2. Gel sample processing and image analysis

Gel sample processing and image analyses as well as particle types and modeled carbon fluxes are described in detail by Durkin et al. (2015; 2021). Here, we focus on the sinking particle size distributions (PSDs) to support interpretations of bulk trap fluxes and summarize the relevant subset of analytical procedures. After the recovery steps outlined above, overlying seawater was vacuumed out of the tubes with gel collectors, leaving behind the last 1–2 cm of water in each collector jar. Gel jars were removed from tubes and then the last layer of seawater was carefully removed via pipette. Identical blank gels kept in the laboratory for the duration of each deployment were treated in the same way as samples. The samples were imaged on board ship with a stereomicroscope (Olympus SZX16) and digital camera (Teledyne Lumenera Infinity 2) at varying magnifications (7×–115×) and focal planes and then frozen. In approximately half of the samples, ship motion precluded high-resolution (50×–115×) imaging at sea, so this step was performed on shore after thawing. In prior studies, the freeze-thaw process did not impact the detection or measurement of particles (Durkin et al., 2021). Median background values from process blanks were subtracted from the images. A thresholding and edge detection algorithm was applied to detect and measure particles in gel images. Particle duplicates detected in multiple focal planes were discarded and then equivalent spherical diameters (D) of particles were computed from their 2D imaged areas as described by Durkin et al. (2015; 2021). Every particle image was sized, counted, and manually classified into a passively sinking particle category or into various nonsinking or "noise" particle categories (e.g., zooplankton swimmers, fibers, imaging noise). Intact zooplankton "swimmers" were presumed to have actively entered the trap (Knauer et al., 1979; Lee et al., 1988; **Table 2**). Blank gels did not contain any particles that could be classified into the passively sinking particle categories identified in the sample gels nor were there any particles classified as "swimmers." In the subsequent analyses described below, we disregarded the nonswimmer, "noise" particles identified in both the samples and blanks, negating the need to subtract the process blanks from the samples.

Particles classified as passively sinking were binned by diameter into logarithmically spaced size bins ranging from 10.7 to 8,192 μm. Similar to the procedure described by Durkin et al. (2015), size bins smaller than 32 μm were computed from particle images detected at 115× magnification, particles 32–90 μm at 50×, particles 90–362 μm at 20×, and particles larger than 362 μm at 7× magnification. These size ranges target the optimal detection limits of the microscope and camera combination at each magnification. This approach eliminates the underestimation of fluxes by particles smaller than the optimal detection limits of each magnification. However, the fluxes of particles smaller than 32 μm detected at 115× appear to be at the limit of the microscope and camera resolution and are likely underestimated (Durkin et al., 2015). Area fluxes (units of μm^2 or $mm^2\ m^{-2}\ d^{-1}$) and number fluxes (units of particles $m^{-2}\ d^{-1}$) were computed, respectively, by normalizing the total projected area of particles, and the number of particles counted, to the imaged area and the deployment length. Differential number fluxes ($N(D)$;

Table 2. Measured bulk fluxes to traps. DOI: https://doi.org/10.1525/elementa.2020.00122.t2

Trap Type[a]	Epoch	Date in 2018 (UTC)	Depth (m)	Uncorrected POC Flux (mmol C m^{-2} d^{-1})		bSi Flux (mmol Si m^{-2} d^{-1})		^{234}Th Flux (dpm m^{-2} d^{-1})		Mass Flux (mg m^{-2} d^{-1})		Passive Area Flux (mm^2 m^{-2} d^{-1})	Corrected POC Flux (mmol C m^{-2} d^{-1})		Swimmer Area Flux (mm^2 m^{-2} d^{-1})	Swimmer Number Flux (individual m^{-2} d^{-1})	Low-Swimmer Subset[a]
				Mean	Uncertainty	Mean	Uncertainty	Mean	Uncertainty	Mean	Uncertainty		Mean	Uncertainty			
SOLO	1	August 15	96	2.71	0.80	0.23	0.01	549	57	89.00	3.76	2,938	1.16	0.80	5,260	3,325	0
SOLO	1	August 15	97	2.83	0.09	0.17	0.01	497	50	83.51	14.77	2,066	0.92	0.77	6,813	3,785	0
APEX	1	August 15	159	4.47[b]	0.77[b]	0.17[b]	0.01[b]	306[b]	23[b]	94.58[b]	10.30[b]	1,491	0.67	0.43	16,465	4,208	0
APEX	1	August 15	209	2.85	0.43	0.10	0.02	193	24	88.42	11.24	1,168	0.45	0.22	11,528	1,525	0
APEX	1	August 15	207	4.35	0.45	0.15	0.01	287	14	90.99	3.93	3,700	0.91	0.27	8,984	3,105	0
APEX	1	August 15	342	1.53	0.19	0.09[b]	0.01[b]	275	39	27.48[b]	6.89[b]	2,212	0.63	0.45	1,628	1,310	0
STT	1	August 15	95	1.65	0.29	0.19	0.02	581	68	61.31	6.29	3,686	1.22	0.32	1,574	3,033	0
STT	1	August 15	145	1.55	0.42	0.19[b]	0.01[b]	585	128	47.74[b]	0.35[b]	NA[c]	1.15	0.43	NA	NA	0
STT	1	August 15	195	0.98	0.08	0.15	0.01	301	61	49.21[b]	5.53[b]	NA	0.70	0.08	NA	NA	0
STT	1	August 15	330	1.94	0.08	0.18[b]	0.01[b]	307	5	67.90[b]	3.45[b]	1,927	0.75	0.08	2,494	1,798	0
STT	1	August 15	500	0.39	0.05	0.08[b]	0.01[b]	120	16	16.49[b]	0.24[b]	2,734	0.39	0.05	704	1143	1
SOLO	2	August 24	101	1.57	0.43	0.15	0.01	236	7	47.19	2.21	1,414	0.59	0.42	2,335	2,714	0
SOLO	2	August 24	103	1.79[b]	0.07[b]	0.13	0.01	186	19	61.12	2.80	1,821	0.56	0.39	3,731	3,647	0
APEX	2	August 24	152	3.86	0.39	0.14	0.02	315	94	69.53	12.89	1,900	0.69	0.30	6,886	4,685	0
APEX	2	August 24	199	6.14	0.30	0.12	0.01	215	12	116.55	8.62	1,658	0.57	0.74	8,436	4,685	0
APEX	2	August 24	203	6.51	1.71	0.18	0.01	386	23	149.76	17.98	935	0.69	0.10	4,917	1,612	0
APEX	2	August 24	337	1.53	0.74	0.10	0.02	175	49	31.60	5.49	654	0.38	1.71	305	824	0
STT	2	August 24	105	1.49	0.55	0.27[b]	0.01[b]	428	57	66.31[b]	17.18[b]	3,599	1.19	0.55	1,014	3,344	0
STT	2	August 24	155	1.70	0.25	0.20	0.01	374	38	66.64	14.72	2,111	0.87	0.25	834	3,242	0
STT	2	August 24	205	1.70	0.75	0.30	0.13	254	19	96.70	26.83	2,489	0.95	0.75	1,976	3,405	0
STT	2	August 24	340	1.27	0.41	0.10	0.02	240	46	58.46	9.81	1,637	0.56	0.41	1,215	1,101	0
STT	2	August 24	510	0.95	0.24	0.22	0.06	412	12	44.72	9.89	2,629	0.95	0.24	1,447	1,060	1
SOLO	3	August 31	104	2.39	0.48	0.61[b]	0.07[b]	678	62	129.65[b]	33.31[b]	4,795	2.39	0.48	840	4,159	1
SOLO	3	August 31	104	2.78	0.57	0.49	0.06	562	46	106.93	8.01	3,484	1.61	0.37	1,141	3,093	0
APEX	3	August 31	147	2.50[b]	0.17[b]	0.36[b]	0.03[b]	391[b]	79[b]	NA	NA	2,525	1.16	0.39	5,966	4,201	0
APEX	3	August 31	198	1.36[b]	0.39[b]	0.18[b]	0.04[b]	149[b]	53[b]	NA	NA	1,752	0.59	0.05	1,487	2,957	0

APEX	3	August 31	334	0.79	0.05	0.08	0.01	168	22	26.33	5.25	1,105	0.40	0.57	425	488	0
STT	3	August 31	105	2.83	0.42	0.81	0.06	1215	63	143.37	13.02	5,495	2.83	0.42	1,034	2,026	1
STT	3	August 31	155	1.70	0.05	0.50	0.02	810	115	80.95	1.54	3,808	1.70	0.05	497	2,374	1
STT	3	August 31	205	1.68	0.20	0.35[b]	0.03[b]	508	53	123.16[b]	45.47[b]	1,944	1.17	0.42	909	1,544	0
STT	3	August 31	340	1.15	0.09	0.19	0.04	443	36	58.85	13.04	1,581	1.15	0.09	931	692	1
STT	3	August 31	510	1.24	0.67	0.20	0.05	619	206	55.89	8.20	2,049	1.24	0.67	421	780	1

SOLO = SOLO-NBST; APEX = APEX-NBST; STT = surface-tethered trap array; NBST = neutrally buoyant sediment traps; UTC = Coordinated Universal Time.

[a]Samples labeled "1" were classified as belonging to the low-swimmer contamination subset. Samples labeled "0" either could not be classified with better than 99% confidence or were part of the contaminated subset.

[b]Means and uncertainties (standard deviation or range) are reported for $n = 3$ splits for uncorrected particulate organic carbon (POC), bSi, ^{234}Th, and mass fluxes except where $n = 2$ as indicated by this footnote. Uncertainties for corrected POC are propagated as described in the text.

[c]NA indicates not available.

units of particles m^{-2} d^{-1} μm^{-1}) were computed by dividing the binned number fluxes by size bin widths. Counting uncertainties were propagated into the different flux estimates. Number and area "fluxes" of swimmers were also computed from the number of pixels occupied by each individual to support the interpretation of bulk elemental fluxes (see Swimmer Correction section).

PSDs were modeled from differential number fluxes by fitting a simple power-law function (Equation 1; e.g., McCave, 1984) to the number fluxes of passively sinking particles using a nonlinear least-squares minimization (Matlab function "fminsearch"; Press et al., 2007):

$$N(D) = A(D_{\mathrm{ref}}) \times (D/D_{\mathrm{ref}})^{S} \quad (1)$$

where $A(D_{\mathrm{ref}})$ gives the PSD amplitude at a reference diameter (D_{ref}), and S gives the PSD slope. The parameter S is sensitive to the particle size range used in fitting the model. We fit Equation 1 to the entire resolvable size spectrum (32–5,792 μm) across all samples collected during the cruise (Figure S1). Uncertainties in the $A(D_{\mathrm{ref}})$ and S parameters were estimated using a Monte Carlo propagation of counting uncertainty.

2.3. Analytical methods

2. 3.1. Particle source funnel modeling

In order to contextualize trap flux measurements within the upper water column, source regions were estimated for particles sinking from the mixed layer to trap collection points (Siegel and Deuser, 1997; Siegel et al., 2008). Velocity fields during the cruise period were determined as follows: Both the *Ride* and *Revelle* carried 150 kHz acoustic Doppler current profilers (ADCPs), which resolved velocity profiles down to approximately 300 m. The *Revelle* additionally carried a 75-kHz instrument, which measured velocities down to approximately 600 m. Velocity profiles from all three instruments were interleaved and decomposed into tidal and inertial components, a low-frequency mean, a linear trend, and a high-frequency residual component. The low-frequency components were similar in magnitude and direction to satellite altimetry-derived geostrophic velocities (AVISO). The spatially gridded, AVISO-derived surface velocities were therefore attenuated with depth in proportion to the attenuation of the time-averaged, low-frequency portion of the current magnitudes from the ADCP. This depth-attenuated AVISO field was then summed with the mean tidal and inertial velocity profile time series. For comparison purposes, a spatially invariant velocity time series was also computed from the *Revelle* ADCP observations.

Statistical source regions for sinking particles were modeled in order to constrain the spatial sensitivity of trap samples. Ten thousand sinking particles were advected backward in time from each point along each sediment trap trajectory (**Figure 1**). The actual location of the STT was used for this determination. NBST paths were modeled as a straight line and at a constant speed between the deployment and resurfacing locations and times. Estimates of particle sinking velocities (SVs) during EXPORTS await future modeling work. Here, source

regions were calculated using representative SVs of 100 and 500 m d^{-1}. Limited shipboard measurements of salp fecal pellets during EXPORTS showed SVs ranging hundreds of meters per day (D Steinberg, personal communication), similar to compilations of SV observations of sinking particles in the literature (e.g., Laurenceau-Cornec et al., 2019). Mean particle trajectories were computed from either the merged AVISO-ADCP velocity grid or the mean *Revelle* velocity time series. The high-frequency residual velocity profile from the decomposition described above was used to spread the particles up and outwards from their collection point at each model timestep, according to Equation 2 (Siegel et al., 2008).

$$u'(t_i) = \left(1 - \frac{\Delta t}{\tau}\right) * u'(t_{i-1}) + \sqrt{2\frac{\Delta t}{\tau}} * \sigma u * r \qquad (2)$$

Above, $u'(t_i)$ is a random velocity imparted to each particle at each timestep, Δt is the model timestep, which is small relative to the assumed decorrelation timescale, τ, set to 10 days following Siegel et al. (2008). The random velocity of the particle, $u'(t_{i-1})$, is set at the previous timestep, σu is the square root of the residual velocity variance, and r is a random number between 0 and 1. Differences between the location and extent of the source regions computed using the AVISO-ADCP and *Revelle* ADCP velocity fields were negligible, and so the AVISO-ADCP-derived source regions were selected for use in subsequent analyses described below.

2.3.2. PSD modeling

The size distribution of sinking particles in the gel traps was used to model the amount of ^{234}Th flux from particles that were too small to fully resolve with the microscope (i.e., smaller than 32 μm) or that were so rare that they had a low probability of collection during days-long trap deployments (see Discussion section, Comparison of Measured and Predicted ^{234}Th Fluxes and Implications for Trap Efficiency section). The mean flux PSD slope was computed by averaging values at each of the five trap depths and extrapolated to give a particle number flux spectrum for sizes ranging from 1 μm to 1 cm (equivalent circular diameter; upper limit chosen to approximate the trap baffle opening). From the modeled flux PSD, we computed the number flux of particles smaller than 32 μm at each depth, converted this value to projected area flux ($A = \pi D2/4$ mm^2 m^{-2} d^{-1} μm^{-1}), and integrated the area flux with respect to particle size. The ^{234}Th flux from this modeled, <32-μm particle pool was estimated using the mean area: ^{234}Th relationship from the trap samples. For comparison to this model, the small-particle ^{234}Th flux was also estimated on a per-trap basis from the observed number fluxes of particles smaller than 32 μm.

The modeled number flux size distribution was also used to compute the mean collection rate (particles d^{-1}) in the summed area of two trap tubes at each trap depth. Using these mean particle collection rates, a Poisson counting model was used to model the size-dependent probability of collecting at least five particles during a 3-day trap deployment (Figure S2). The number flux of particles with a less than 5% probability of collection (at the five particles per 3 days threshold) was computed from the counting model. This hypothetical number flux was integrated with respect to particle size, converted to an area flux, and used to estimate ^{234}Th flux following the same procedure as described above.

2.3.3. Export ratios and transfer efficiency calculations

The Ez-ratio is defined as the export flux of carbon from a reference depth, ideally the base of the euphotic zone or mixed layer, whichever is deeper, divided by the net primary production (NPP) integrated to that depth. The 100-m transfer efficiency (T_{100}) is the downward flux of carbon at 100 m below the reference depth, divided by the export flux at the reference depth. We computed the Ez-ratio and T_{100} metrics (Buesseler and Boyd, 2009; Buesseler et al., 2020b) from our sediment trap data on an epoch-by-epoch basis as well as over the entire cruise. Depth-integrated NPP was determined using the well-established ^{14}C-based approach, following sample processing details reported by Fox et al. (2020), but with the addition of trace-metal clean techniques during all sample handling. Shipboard ^{14}C bottle incubations were carried out for 24 h at light levels corresponding to targeted collection depths ranging from the surface to the 1% photosynthetically available radiation (PAR) depth, around 70 m. The volumetric NPP rates were then integrated to different depths. Here, we report integrated NPP to a depth of 100 m, and use this as our reference depth for Ez-ratio and T_{100} calculations. While the shallowest sediment traps were about 12 m above the 0.1% light level (see below), this choice of reference depth avoids additional uncertainty associated with depth-interpolation of trap fluxes. Uncertainties in single-epoch NPP, Ez-ratio, and T_{100} values were propagated from the standard deviation among the replicate measurements in each trap depth band. For the cruise-long average, we report the mean and uncertainty propagated from standard deviations in each trap depth band, over all three epochs ($n = 7$ for NPP, $n = 8$ or 9 for trap fluxes).

3. Results

3.1. Trap deployments

A weak, anticyclonic mesoscale circulation dominated the mean trap motions during each deployment cycle (**Figure 1**; Siegel et al., n.d.). Superimposed on this larger pattern, the STT array was advected by inertial (period 18 h) and tidal motions and wind drag. While only the deployment and resurfacing locations were available for the NBSTs, they can be assumed to have been similarly affected by inertial and tidal oscillations. Compared to the NBSTs, the STT array drifted further to the north in Epoch 1, to the east in Epoch 2, and to the southeast in Epoch 3 (**Figure 1**). NBSTs had single-cycle endpoint-to-endpoint drift distances ranging from 4.8 to 21.1 km (**Table 1**), consistent with observed current speeds (Siegel et al., n.d.). The STT endpoint-to-endpoint distance (ranging from 16.0 to 30.4 km) was always greater than that of co-deployed NBSTs (except in the single case where an NBST took two cycle

periods to resurface; **Table 1**; Estapa et al., 2020). In situ velocities measured continuously every 10 min at the base of the STT array (Figure S3) had means and standard deviations of 6 $\pm$ 3 cm s^{-1} (Epoch 1), 4 $\pm$ 2 cm s^{-1} (Epoch 2), and 6 $\pm$ 3 cm s^{-1} (Epoch 3).

During the cruise, the depth of the euphotic zone determined from radiometer profiles conducted aboard the *Revelle* had a mean and standard deviation of 112 $\pm$ 7 m (0.1% of surface PAR, $n = 11$), while the mixed layer was 31 $\pm$ 4 m ($n = 227$; using a 0.1 kg m^{-3} criterion) during the sampling period (Siegel et al., n.d.). Prior work supports the interpretation of sinking particle flux data with reference to the primary production zone depth, which is defined as the depth where *in vivo* chlorophyll fluorescence drops to 10% of its maximum value (Owens et al., 2015). This depth, computed from daily chlorophyll fluorescence (FLNTU, WET labs Inc.) profiles of the Lagrangian float followed by the *Revelle*, was 116 $\pm$ 3 m, consistent with the 0.1% PAR depth and with other work supporting the use of a 0.1% PAR definition as the export reference depth (Marra et al., 2014; Buesseler et al., 2020b). As discussed above, the NBST deployment depths and the STT depths in Epoch 1 were targeted at 95, 145, 195, 330, and 500 m, while the STT depths in Epochs 2–3 were 10 m deeper. We have therefore grouped together all traps deployed in the same 10-m interval. For brevity, we refer below to these trap depth bands as 100, 150, 200, 335, and 505 m.

3.2. Bulk fluxes

3.3.1. Swimmer correction

Sediment trap samples were highly impacted by zooplankton "swimmers," with tens of milliliters of biomass removed in some cases. Often more swimmer material was removed from samples than the passive flux material left behind, with NBSTs more greatly impacted by swimmers than STTs (Figure S4). Qualitatively, the bulk of the swimmer biomass manually removed from samples was from *Themisto* and *Vibilia* amphipods (D Steinberg, personal communication). Large numbers of copepods and pteropods were also removed. Passively sinking material adhering to swimmers was carefully separated and returned to the bulk sample. The relative variability of swimmer fluxes before and after picking was computed as the relative difference between two traps, or relative standard deviation among three traps, deployed at the same time and depth. Swimmer area fluxes always showed more relative variability than bulk POC fluxes to the same platforms measured after manual swimmer removal (**Figure 2**). In addition to our visual observations under magnification, this difference suggests that picking was successful at separating swimmers larger than the screen size of 335 μm from passively sinking particles. However, both the bulk compositional characteristics of the sinking flux and visual observations of picked screens, gel samples, and filter splits (H Close, personal communication; Figure S4) suggested that swimmer removal was incomplete. This was likely due to material shed from larger swimmers (such as amphipod eggs that were frequently observed and difficult to remove manually due to their fragility and small

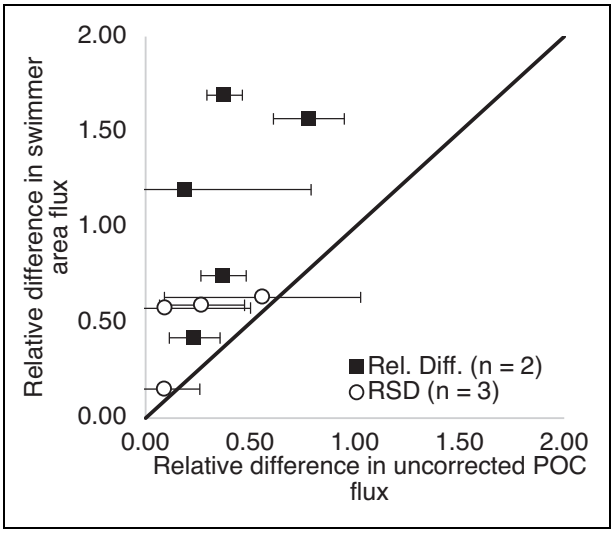

Figure 2. Relative variability in measures of swimmer flux. Relationship between measures of relative variability in swimmer area flux to gels, and relative variability in particulate organic carbon (POC) flux to bulk traps prior to statistical swimmer correction (see text). Black squares show relative differences (relative difference) between pairs of traps co-deployed at the same target depth, which is defined, for trap pairs, as the absolute difference between the two measurements, divided by the mean. White circles show relative standard deviations (RSDs) among sets of three traps co-deployed at the same target depth. For triplicates, the RSD is the standard deviation among the three measurements divided by their mean. Error bars show propagated, split-to-split uncertainty from single platforms. The 1:1 line is shown for reference (solid black). DOI: https://doi.org/10.1525/elementa.2020.00122.f2

sizes), swimmers that were small enough to pass through the screen, and possibly from unrecognized, fragmented, or cryptic swimmers (Michaels et al., 1990).

Relationships among the bulk elemental fluxes and magnitudes of some fluxes suggested nonnegligible contributions by swimmers to certain analytes (total and inorganic carbon, nitrogen, phosphorus, and total mass; **Figure 3**). For instance, ratios of carbon to ^{234}Th in STT and NBST trap samples ranged from 2.1 to 29 μmol dpm^{-1}, with a median of 5.4 μmol dpm^{-1}. Previous work in the region has shown that C:^{234}Th values are almost always less than 6 μmol dpm^{-1} (Charette et al., 1999; Kawakami et al., 2010; Mackinson et al., 2015). The higher values observed here are consistent with contamination by zooplankton, which typically have high C:^{234}Th ratios (Coale, 1990; Buesseler et al., 2006; Passow et al., 2006). The organic carbon (OC) weight fraction of the total mass flux ranged from 0.17 to 0.68 with a median of 0.34. Several samples had OC weight fractions above 0.5 (**Figure 3b**), consistent with enhanced contributions from components such as lipids and proteins (Hedges et al., 2002). We found that samples with high C:^{234}Th and high OC weight fractions also had high area fluxes of zooplankton swimmers

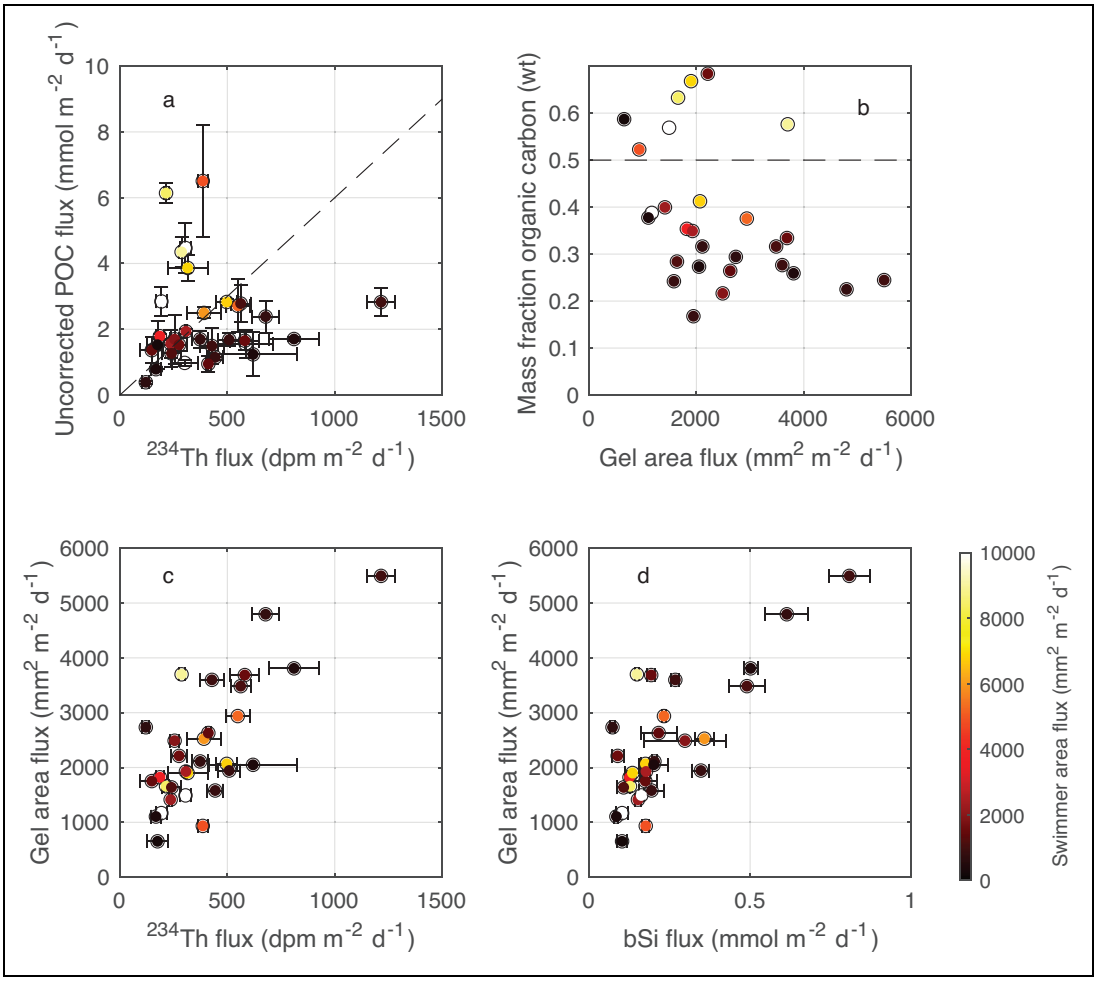

Figure 3. Bulk flux compositional ratios used for swimmer correction. Property-property plots for bulk flux samples illustrate the properties used to identify uncontaminated samples for statistical swimmer correction. In all panels, symbol colors correspond to the cross-sectional area "flux" of swimmers in gel collectors. Panel (a): Particulate organic carbon (POC) flux versus ^{234}Th flux, no significant correlation. Dashed line shows POC:^{234}Th = 6 μmol dpm^{-1}. Panel (b): Mass fraction of organic carbon (see text) versus area flux of nonswimmer particles, $R^2 = .15$, $p < .05$. Dashed line shows mass fraction OC = 0.5. Panel (c): Area flux of nonswimmer particles versus ^{234}Th flux, $R^2 = .56$, $p < 10^{-5}$. Panel (d): Area flux of nonswimmer particles versus biogenic silica (bSi) flux, $R^2 = .62$, $p < 10^{-6}$. Error bars indicate plus or minus one standard deviation ($n = 3$) or the range ($n = 2$) of directly measured splits (see **Table 2**). DOI: https://doi.org/10.1525/elementa.2020.00122.f3

to the gel trap on the same platform (**Figure 3a** and **b**). Swimmer-impacted analytes also showed high fluxes and inter-platform variability in the upper 195 m of the water column. In contrast, we found that fluxes of ^{234}Th and bSi appeared to be less influenced by swimmer contributions as they were well-correlated to the area fluxes of nonswimmer particles to the gel traps (**Figure 3c** and **d**).

To correct for the additional POC flux contributed by swimmer material that passed through the 335-μm mesh, a statistical correction procedure was applied (**Figure 4**; Text S1). An unsupervised classification (Gaussian mixture cluster analysis; Press et al., 2007) was used to identify the subset of samples with high covariance among the following compositional ratios: bSi:POC, ^{234}Th:POC, area:POC, and mass:POC. We assumed that these samples, which spanned the whole range of trap depths, were unlikely to be contaminated by swimmer material. The mean bSi:POC, ^{234}Th:POC, and area:POC ratios from those samples were used to generate three independent, passive-only (i.e., swimmer-free) estimates of POC flux for the remainder of the samples. The estimated passive POC flux was insensitive to whether mean or depth-dependent compositional ratios were used, so we used the mean. Swimmer-corrected POC fluxes reported below were subsequently computed by averaging the three independent estimates. The uncertainty of this corrected POC flux is reported as the larger of either the standard deviation among the three estimates or the original observational uncertainty (mainly split-to-split variability; **Table 2**). The estimated contribution of swimmer material smaller than 335 μm (**Table 2**; Figure S4) was computed as the difference between the measured and corrected POC flux. Here and below, we use the terms "swimmer-corrected," "swimmer POC," and "swimmer POC flux" in reference to quantities stemming from our statistical correction for swimmer material that passed the 335-μm mesh, and not to refer

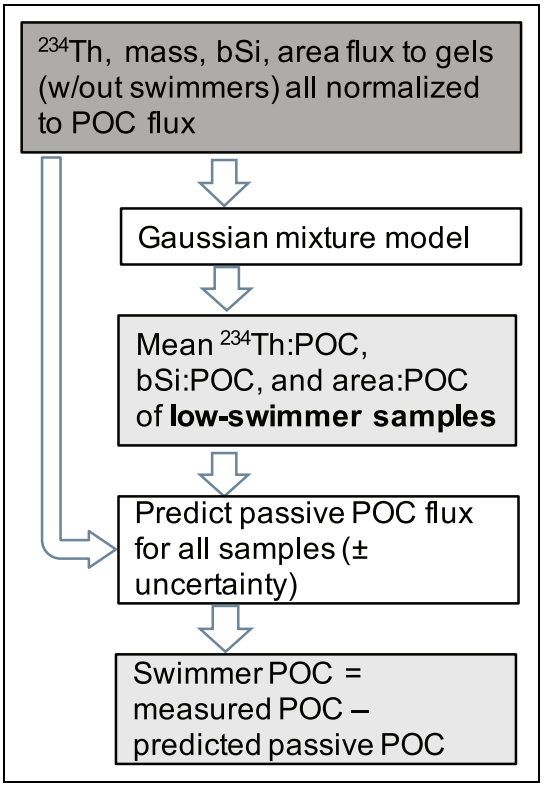

Figure 4. Flowchart illustrating the modeling process for statistical swimmer correction. Dark gray box indicates observed quantities. Light gray boxes indicate modeled quantities, and white boxes indicate model steps. bSi = biogenic silica; POC = particulate organic carbon. DOI: https://doi.org/10.1525/elementa.2020.00122.f4

to larger swimmers that were removed manually from the screen prior to splitting and filtering.

Calculated swimmer POC contributions from material smaller than 335 µm in the screened and manually picked samples (**Table 2**) correlated positively with the area flux of swimmers of all sizes to the gel traps ($R^2 = .53$, $p < 10^{-5}$) but were not significantly related to area fluxes of swimmers smaller than 335 µm. Both the calculated swimmer POC correction and the total area flux of swimmers to gel traps were much larger in the NBSTs than in the STTs (Figure S4). However, the area fluxes of swimmers smaller than 335 µm were similar in NBSTs and STTs and comprised only a small fraction (median 6%) of the total swimmer area in the gels (Figure S4). These findings suggest that most of the swimmer material passing through the mesh originally entered the traps with larger swimmers and was detached during bulk sample handling. Swimmer POC from material smaller than 335 µm contributed between 0 and 91% of the measured, uncorrected POC flux (mean ± standard deviation of 45 ± 31%, $n = 32$). Above 200 m, significant differences were observed between trap types in Epochs 1 and 2 (but not Epoch 3), with much higher swimmer POC contributions observed in NBST samples (paired-sample t test, 95% confidence; **Table 2**). No epoch-to-epoch differences were observed in contributions of <335 µm swimmer POC in the STTs, and for NBSTs only Epochs 1 and 3 differed significantly from one another (paired-sample t test, 95% confidence). The mean elemental ratios of the swimmer-free sample subset are reported below. Corrected profiles of the other swimmer-contaminated analytes besides POC (*N*, *P* mass, PIC) can be estimated by scaling passive POC flux estimates by the appropriate elemental ratios.

3.2.2. Flux profiles, bulk composition, and BCP efficiency

The corrected sediment trap-derived POC fluxes observed here were low and somewhat variable, with a cruise-wide average (± standard deviation, $n = 9$) of 1.38 (± 0.77) mmol C m^{-2} d^{-1} at the uppermost trap depth (100 m), attenuating significantly to 0.76 (± 0.20) mmol C m^{-2} d^{-1} by a depth of 200 m ($n = 8$; t test, 95% confidence; **Figure 5**; **Table 2**). Surface-tethered sediment traps generally had a higher POC flux than NBSTs deployed at the same time and depth (39 ± 18% overall, Type-II linear regression, $n = 12$). POC fluxes also varied from epoch to epoch, increasing significantly (t test, 95% confidence) from 0.94 (± 0.30, $n = 6$) mmol C m^{-2} d^{-1} in Epochs 1 and 2 to 2.27 (± 0.61, $n = 3$) mmol C m^{-2} d^{-1} in Epoch 3. All nonswimmer impacted fluxes (bSi, ^{234}Th, and area flux to gels) also increased significantly at 100 m from Epochs 1 and 2 to Epoch 3 (**Figure 5**). Significant epoch-to-epoch changes were not observed below 100 m, except for bSi at 145 m where fluxes in Epoch 3 increased to 0.43 (± 0.10, $n = 2$) mmol Si m^{-2} d^{-1} from 0.17 (± 0.03, $n = 4$) mmol Si m^{-2} d^{-1} in Epochs 1 and 2.

We assumed that the samples determined to be uncontaminated by POC from swimmers also had negligible swimmer contributions to measured *N*, PIC, and mass fluxes. We computed median compositional ratios from this small subset ($n = 7$; **Table 2**), which spanned all trap depths, epochs, and trap types, but which was not sufficient to examine variability within those categories. The median (interquartile range) of the POC: *N* molar ratio determined for this subset was 7.0 (± 1.5), the PIC: POC molar ratio was 0.035 (± 0.011), and the POC:mass ratio was 0.25 (± 0.03). The POC:*P* molar ratio was 264 (± 187), although this ratio was higher than observed in samples from in situ pumps (M Roca-Martí, personal communication) and could indicate enhanced solubilization of *P* prior to sample filtration (e.g., Lamborg et al., 2008). The bSi:POC molar ratio increased from 0.15 (± 0.03, $n = 2$) in Epoch 1 to 0.29 (± 0.02, $n = 4$) in Epochs 2 and 3 (**Figure 6b**). The POC:^{234}Th ratio did not change significantly among the three epochs and had a mean of 2.2 (± 0.2) µmol dpm^{-1}, consistent with >51 µm particulate samples collected via in situ large-volume pumps (**Figure 6a**; Buesseler et al., 2020a).

Epoch averages of NPP integrated to the uppermost trap depth ranged from 13.0 to 14.1 mmol C m^{-2} d^{-1} with a cruise mean of 13.8 (± 1.9, $n = 7$) mmol C m^{-2} d^{-1} (**Table 3**). We use the Ez-ratio (here computed as the flux at the reference depth, 100 m, normalized to NPP) and the T_{100} (flux at 200 m normalized to flux at 100 m) as metrics to describe the BCP efficiency (Buesseler and Boyd, 2009; Buesseler et al., 2020b). We found Ez-ratios ranging from

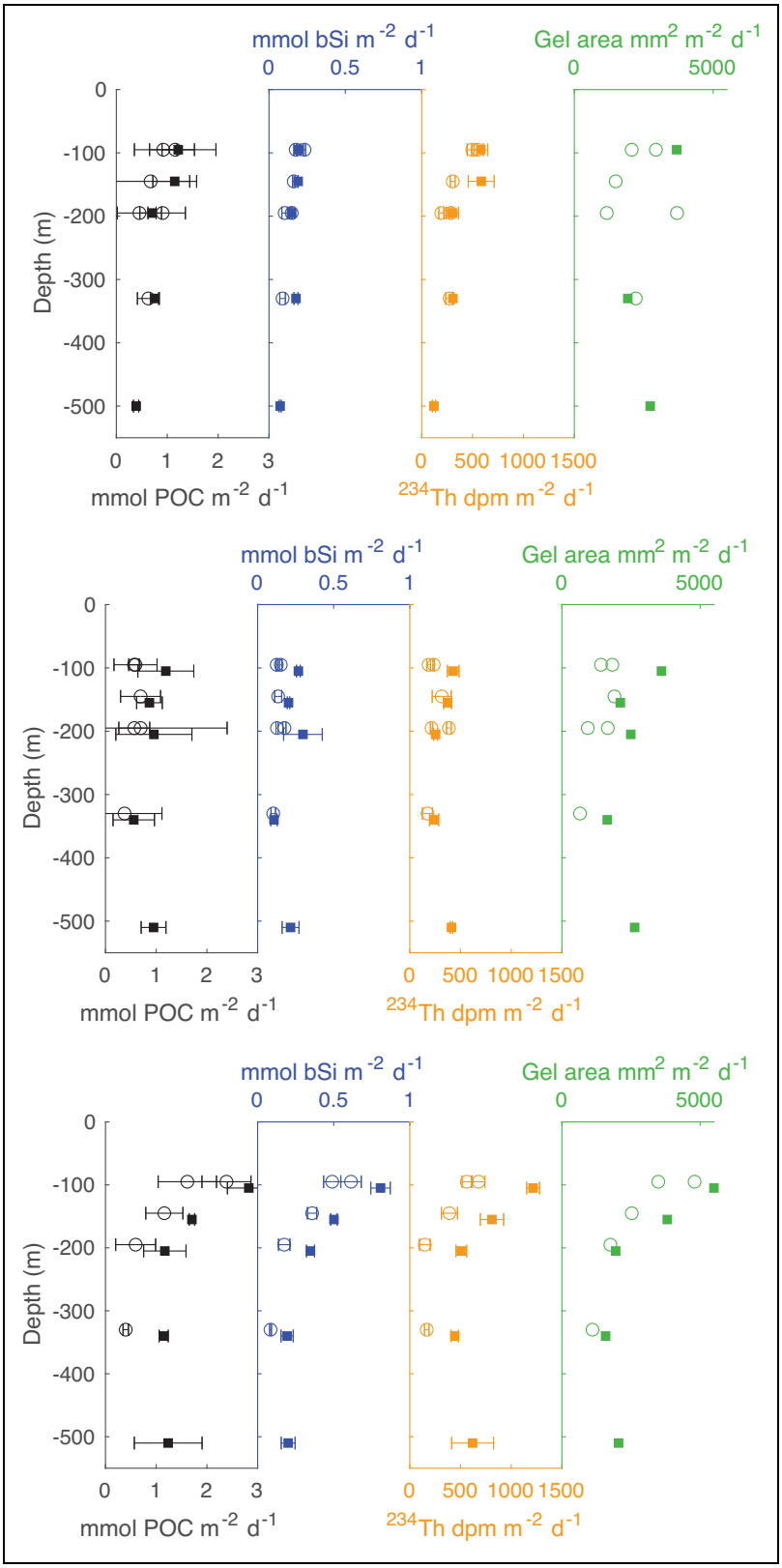

Figure 5. Fluxes of swimmer-corrected particulate organic carbon, biogenic silica (bSi), ^{234}Th, and passively sinking area in gels. Open circles show fluxes to neutrally buoyant sediment traps, and filled squares show fluxes to surface-tethered traps. Panels a, b, and c show Epochs 1, 2, and 3, respectively. Error bars indicate plus or minus one standard deviation ($n = 3$) or the range ($n = 2$) of directly measured splits (see **Table 2**). POC = particulate organic carbon; bSi = biogenic silica. DOI: https://doi.org/10.1525/elementa.2020.00122.f5

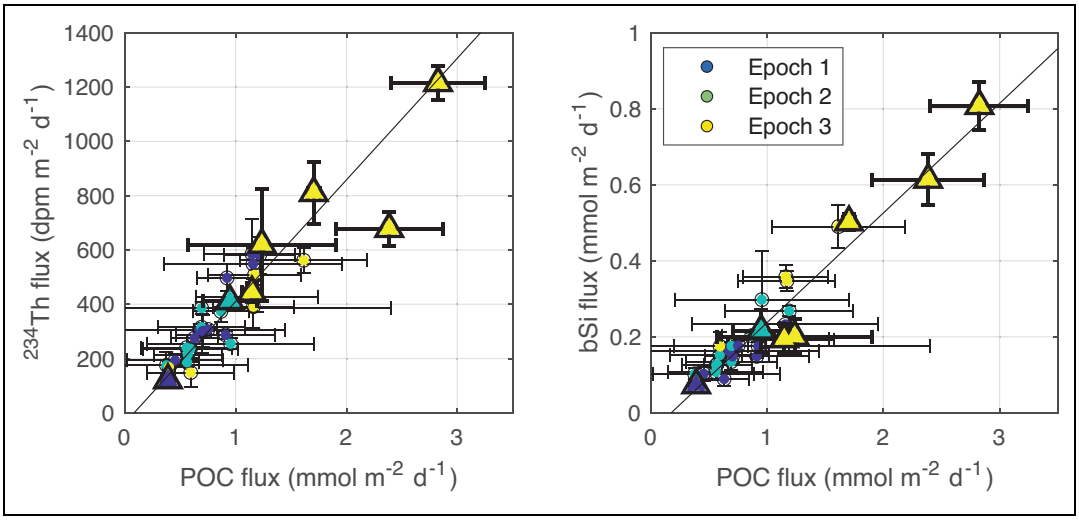

Figure 6. Thorium-234 and biogenic silica (bSi) ratios to particulate organic carbon (POC). Colors indicate epoch and correspond to **Figure 1**. Samples from the low-swimmer subset (see text and **Table 2**) are shown in larger triangles with heavy outlines. Small swimmer-corrected samples are shown with circles. (Left) ^{234}Th versus swimmer-corrected POC. Mean POC:^{234}Th ratio (± standard deviation) computed by Type-II linear regression is 2.2 (± 0.2) µmol dpm^{-1}; $R^2 = .86$, $p < 10^{-13}$, $n = 32$. (Right) bSi versus swimmer-corrected POC. Mean bSi:POC ratio (mol/mol) computed by Type-II linear regression is 0.29 (± 0.02); $R^2 = .90$, $p < 10^{-15}$, $n = 32$. Error bars indicate plus or minus one standard deviation ($n = 3$) or the range ($n = 2$) of directly measured splits (see **Table 2**). DOI: https://doi.org/10.1525/elementa.2020.00122.f6

0.06 to 0.18 with a cruise-long mean of 0.10 (± 0.06; propagated from $n = 7$ NPP measurements and $n = 9$ POC flux measurements at 100 m). The T_{100} values for POC ranged from 0.4 to 0.9 with a mean of 0.55 (± 0.35; $n = 8$ POC flux measurements at 200 m; **Figure 7**; **Table 3**). We also computed T_{100} values for the fluxes without apparent swimmer contamination (bSi, ^{234}Th, and gel area; **Table 3**; $n = 3$ except $n = 2$ in Epoch 2 at 200 m). For bSi, T_{100} ranged from 0.4 to 1.1 with a mean of 0.6 (± 0.5); for ^{234}Th, T_{100} ranged from 0.4 to 1.0 with a mean of 0.5 (± 0.4); and for gel area flux, T_{100} ranged from 0.4 to 0.8 with a mean of 0.6 (± 0.4). Among all analytes, T_{100} varied the most in Epoch 1, was largest in Epoch 2, and varied the least and was lowest in Epoch 3 (**Table 3**).

3.3. Size distribution of sinking particles

PSD slopes (± propagated particle counting uncertainty) of sinking particles ranged from −2.15 (± 0.07) to −3.31 (± 0.16). For comparison, an equal volume distribution across all size classes may arise when mass redistribution among particles reaches a steady state, which would result in a theoretical PSD slope of −4 (Sheldon, 1972). Observed size distribution slopes of marine suspended particles typically fall between −2 and −4 (e.g., Guidi et al., 2009). Our sinking particle observations are therefore consistent with an increase in larger versus smaller particles, relative to typical distributions of suspended particles. The slope parameter S also generally decreased (became steeper) with increasing depth from 100 to 335 m, indicating a shift from larger to smaller particles over that depth range, albeit with substantial variability, consistent with the observations of Guidi et al (2009; **Figure 8**). Among all samples, the median particle size (i.e., the equivalent spherical diameter calculated from the median area) ranged from 75 to 1,461 µm with a median of 282 µm. Particles smaller than 51 µm in diameter contributed between 0.57% and 42% of the total area flux, with a median of 11%. No significant trends in the median particle diameter or contribution of particles smaller than 51 µm were observed as a function of depth.

In spite of the relative importance of the largest particles to overall fluxes, they were not numerically abundant in the gel traps. Among size bins with median diameters larger than 437 µm, some samples had fewer than 10 particles (i.e., relative counting error greater than 32%) collected during a deployment. In size bins larger than 874 µm, some samples had zero particles collected. No particles larger than 5,792 µm were observed. The power-law model (Equation 1) gave a reasonable fit to the particle size data over the entire size range, with relative uncertainties in S determined by Monte Carlo propagation of counting uncertainty ranging from 2% to 10% (**Figure 8**). However, the observed size distributions included local minima and maxima that deviated from the model (Figure S1).

The estimated fluxes of ^{234}Th carried by observed particles smaller than 32 µm had a mean (± standard deviation) of 26 (± 13, $n = 30$) dpm m^{-2} d^{-1}. The modeled fluxes of ^{234}Th carried by 1–32 µm particles, computed by extrapolation of number flux size distributions to small sizes not well-resolved by microscopy, were larger and ranged from 119 to 376 dpm m^{-2} d^{-1}. Averaging the observations by depth and taking the difference from the model led to a conservative estimate of "missed" small particle ^{234}Th flux ranging from 89 to 350 dpm m^{-2} d^{-1}, with the maximum observed at 150 m and the minimum

Table 3. Particulate organic carbon (POC) fluxes, export ratios, and POC, biogenic silica, and ^{234}Th transfer efficiencies.[a] DOI: https://doi.org/10.1525/elementa.2020.00122.t3

		Fluxes (mmol C m^{-2} d^{-1})				Transfer Ratio (T_{100})[b, c]			
Sampling Period	Sampling Period (2018)	POC at 100 m	POC at 200 m	NPP[d]	Export Ratio	POC	bSi	^{234}Th	Area[e]
Epoch 1	August 15–20	1.10 (0.16, n = 3)	0.69 (0.23, n = 3)	14.09 (1.76, n = 2)	0.08 (0.01)	0.63 (0.23)	0.67 (0.16)	0.48 (0.11)	0.84 (0.66)
Epoch 2	August 24–28	0.78 (0.35, n = 3)	0.74 (0.20, n = 3)	14.03 (2.81, n = 3)	0.06 (0.03)	0.94 (0.50)	1.10 (0.67)	1.01 (0.55)	0.74 (0.51)
Epoch 3	August 31 to September 5	2.27 (0.61, n = 3)	0.88 (0.41, n = 2)	13.01 (2.70, n = 2)	0.17 (0.06)	0.39 (0.21)	0.41 (0.22)	0.40 (0.35)	0.40 (0.09)
Cruise[c]	August 15 to September 7	1.38 (0.77, n = 9)	0.76 (0.24, n = 8)	13.81 (1.92, n = 7)	0.10 (0.06)	0.55 (0.35)	0.56 (0.47)	0.52 (0.35)	0.60 (0.38)

POC = particulate organic carbon; NPP = net primary production; bSi = biogenic silica.

[a]All values reported as mean (with standard deviation).

[b]T_{100} = flux at 200 m/flux at 100 m (see text).

[c]Transfer ratios of bSi, ^{234}Th, and area flux have standard deviations computed from n = 3 measurements each at 100 m and 200 m, except n = 2 at 200 m in Epoch 3.

[d]Depth-integrated NPP computed to the upper trap depth (100 m), which was slightly shallower than the 0.1% light level (see text).

[e]"Area" refers to the total cross-sectional area flux of passively sinking particles into the gel traps (see text).

Figure 7. Export ratios from traps versus transfer efficiency of flux to a depth 100 m below. Metrics were computed at the upper trap depth (at 100 m), slightly above the 0.1% photosynthetically available radiation depth. Radii of the ellipses show the standard deviations of T100 and the Ez-ratio. Filled ellipses show values within each sampling epoch with colors as in **Figure 1**. Open ellipses show the cruise mean as measured with sediment traps (black), and as predicted from ^{234}Th deficits and water column particulate organic carbon:^{234}Th ratios (gray; Buesseler et al., 2020a). Figure design after Buesseler and Boyd (2009) and Buesseler et al. (2020b). DOI: https://doi.org/10.1525/elementa.2020.00122.f7

at 500 m. The modeled ^{234}Th flux carried by rare particles with less than 5% probability of reaching a collection threshold of five particles in 3 days ranged from 120 to 456 dpm m^{-2} d^{-1}, with the maximum observed at 100 m and the minimum at 330 m. The summed, modeled fluxes of ^{234}Th carried by rarely collected and 1–32 µm particles ranged from 287 to 567 dpm m^{-2} d^{-1}.

Durkin et al. (2021) classified passively sinking particles imaged in the gel traps that were approximately 10 µm or larger into nine morphological categories. Using literature values and prior, independent field measurements, modeled, size-dependent carbon contents were assigned to each particle class. The details of this model are presented elsewhere (Durkin et al., 2021), but we summarize a subset of the results here in order to support comparisons to the measured bulk fluxes. The POC fluxes modeled from particles identified in the gel traps agreed with the measured POC fluxes presented here (**Figure 9**; see also figure 13 in Durkin et al., 2021), with a linear regression ($\pm$ parameter 95% confidence intervals) of *Modeled POC* = 1.2 ($\pm$ 0.6) × *Measured POC* + 0.006 ($\pm$ 0.7; R^2 = .38, $P < 10^{-3}$). When large but infrequent contributions from salp fecal pellets were excluded from the modeled POC fluxes, the scatter in the relationship improved, but the slope did not change (R^2 = .73, slope = 1.2 $\pm$ 0.3).

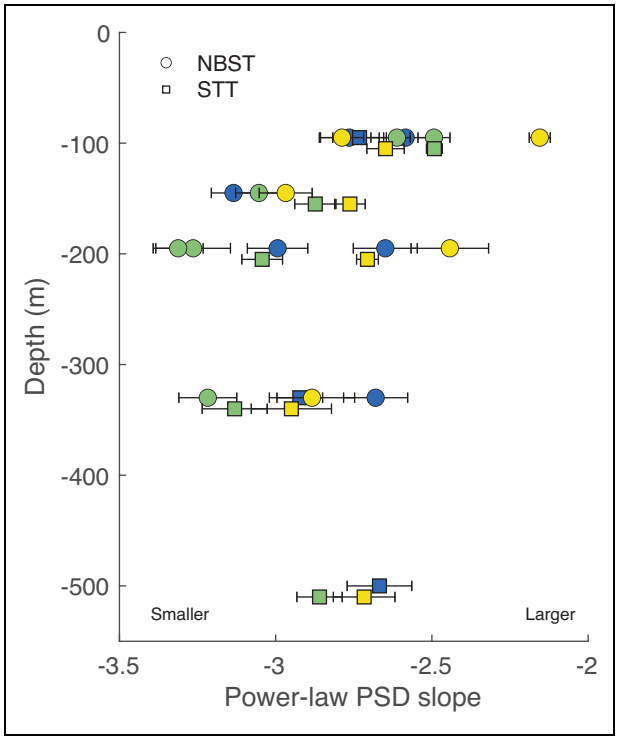

Figure 8. Power-law particle size distribution (PSD) slopes measured from particles in gel traps. Colors correspond to epoch and match **Figure 1**. Circles show neutrally buoyant sediment trap (NBST) samples and squares show surface-tethered trap (STT) samples. Less negative power-law slopes for PSD correspond to larger particles, and more negative slopes correspond to smaller particles. In general, passively sinking particle size decreased with depth through 335 m but then increased slightly at 505 m. Error bars show particle counting uncertainty propagated into the PSD model using a Monte Carlo technique (see text). DOI: https://doi.org/10.1525/elementa.2020.00122.f8

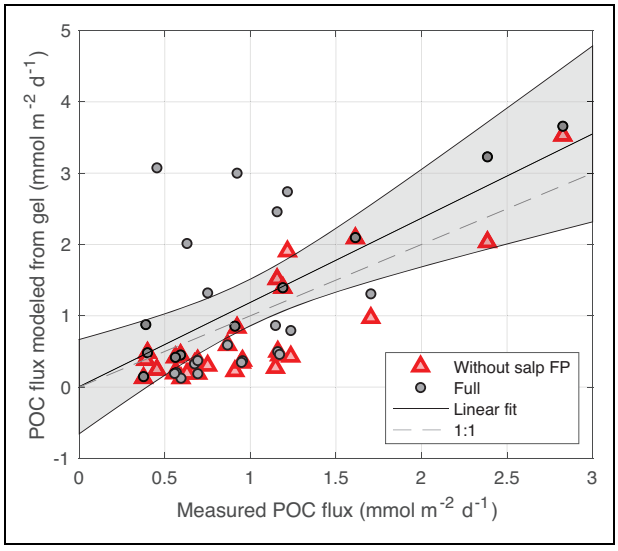

Figure 9. Measured and independently modeled particulate organic carbon (POC) fluxes. Comparison of independently modeled POC flux based on particle identities in gels (Durkin et al., 2021) to swimmer-corrected bulk POC fluxes measured in this study. Modeled fluxes by all particle types (open black circles) showed larger scatter relative to measurements than after contributions by rare salp fecal pellets (FP) were removed (red dots). A linear regression of modeled versus measured fluxes (black line) gave $y = 1.2\ (\pm\ 0.6)\ x + 0.006\ (\pm\ 0.7)$, $R^2 = .38$, $P < 10^{-3}$. The gray-shaded area shows the 95% confidence interval of the fit. The 1:1 line (gray dashed) is shown for reference. DOI: https://doi.org/10.1525/elementa.2020.00122.f9

3.4. Trap source regions

Consistent with similar source region modeling work in prior studies (e.g., Siegel et al. 2008), trap source areas increased with trap depth (Figure S5). Areas of source regions were similar between NBST and STT traps, likely because the mean flow was small relative to higher frequency motions responsible for spreading and divergence of the source regions. For modeled particles sinking at 100 m d^{-1}, source regions were offset from trap locations by 3–8 km and the diameters of source regions ranged from 9 to 20 km, both increasing with depth. In contrast, source regions for particles sinking at 500 m d^{-1} had offsets ranging from 0.9 to 1.7 km and diameters of only 0.7–4.4 km. The STT and NBST source regions diverged from one another at 100 m in Epochs 2 and 3, but overlapped during part of Epoch 1, and at depths below 100 m in all epochs. The trap source regions for particles sinking at 100 m d^{-1} were generally well-sampled by conductivity-temperature-depth (CTD) casts from the ships, although casts from the *Ride* in Epoch 2 were not as dense within the source regions because the ship's sampling effort was extended over a larger area (Siegel et al., n.d.). Source regions for particles sinking at 500 m d^{-1} were not well-sampled by CTD casts from the *Ride* because of their much smaller extents.

4. Discussion

4.1. Method—method intercomparisons

Sediment traps have been a standard tool for measuring sinking particle flux for decades, yet uncertainties about their collection efficiencies and biases relative to other methods still persist. These issues were reviewed comprehensively by Buesseler et al. (2007). More recently, Lamborg et al. (2008), Owens et al. (2013), and Baker et al. (2020) reported field intercomparisons of different trap designs. The sediment trap deployments conducted here take into account many of the lessons learned in the earlier studies: minimizing hydrodynamic bias by utilizing NBSTs alongside STTs (Buesseler et al., 2007), employing cylindrical trap tubes to avoid funnel effects associated with conical traps (Baker et al. 2020), collecting process blanks for every analyte to control for the effects of sample handling (Owens et al., 2013), and ensuring that STTs were deployed below the mixed layer (Owens et al., 2013). Sediment traps remain the only way to isolate and concentrate sinking particles from the suspended pool for laboratory analysis. However, because there is no absolute standard for sinking particle fluxes, the only way to

evaluate the accuracy of sediment traps is to compare observations to other methods. The EXPORTS field campaign is one of the most comprehensive efforts to date in terms of simultaneous, independent particle flux measurements. In addition to the direct measurement of bulk carbon fluxes reported here, the program included sinking particulate carbon fluxes estimated from gel trap imagery (Durkin et al., 2021), from water column ^{238}U-^{234}Th (Buesseler et al., 2020a) and ^{210}Pb-^{210}Po disequilibria (Roca-Martí et al., 2020) and from Marine Snow Catcher samples (Romanelli et al., 2020). We, therefore, have an unprecedented opportunity to explore the underlying causes for mismatches among methods as well as to describe the functioning of the BCP in this subpolar gyre setting.

4.1.1. Trap–trap reproducibility and platform differences

This study was consistent with prior observations of an approximate 10% overcollection of sinking POC flux by STTs relative to NBSTs (Estapa et al., 2020). The STT array was subject to wind stress on the surface buoy, which led to its divergence from the co-deployed NBSTs in all epochs (**Figure 1**). However, the measured relative velocities at the base of the STT array in each epoch mostly remained below the 10 cm s^{-1} threshold at which hydrodynamic effects have been shown to become important (Buesseler et al., 2007). In addition, the size distributions of particles collected by the two trap types were similar (**Figure 8**), qualitatively suggesting that hydrodynamic sorting effects played a minimal role. POC fluxes from replicate NBSTs (two platforms co-deployed at the same depth) were determined five times during the cruise, and no significant differences were observed (two-sample *t* test, 95% confidence). Alternatively, in this study, the higher fluxes measured by the STTs versus NBSTs may have arisen from spatial displacements between the trap types, particularly in Epoch 3 (**Figure 1**; **Table 2**), or from effects of the different trap designs (Baker et al., 2020).

4.1.2. Statistical swimmer correction

An independently calibrated, particle-identity-based POC flux model, which took as input only the numbers, sizes, and identities of nonswimmer particles in the gel traps, agreed well with the swimmer-corrected, bulk POC fluxes presented here (Size Distribution of Sinking Particles section, **Figure 9**; Durkin et al., 2021). The good agreement between these two independent estimates of sinking particle POC flux to the traps, and the fact that the gel POC flux model is insensitive to swimmers, suggests that the statistical swimmer correction procedure applied to the bulk flux measurements was robust and that manual swimmer removal from bulk samples did not inadvertently remove passively sinking POC from the sample. Additional, qualitative support for the robustness of the correction is shown by its ability to account for widely varying levels of swimmer contamination in NBSTs versus STTs (Figure S4).

The contamination of sediment trap samples by active swimmer intrusion is a decade-old problem (e.g., Knauer et al., 1979; Lee et al., 1988). Solutions have run the gamut and include the following: sediment trap design innovations (e.g., "the labyrinth of doom" and "indented rotating sphere" traps; Coale, 1990; Peterson et al., 2005), simple size-based separations such as those used in the Hawaii Ocean Time-series (HOT) program (Karl et al., 1990) and by this group at sites where that approach has been validated (Owens et al., 2013; Estapa et al., 2017), hybrid approaches where swimmers above a certain size are removed manually (Baker et al., 2020; this study), and the labor-intensive, fully manual swimmer removal techniques regularly employed by the Bermuda Atlantic Time-series Study (BATS) program (Knap et al. 1997). The types and intensity of swimmer intrusion into sediment traps are highly variable and difficult to predict in advance of deployments. For instance, the NBSTs employed in this study attracted more swimmers than did co-deployed STTs (Figure S4), even though in prior work the reverse has occurred (Buesseler et al., 2000). Owens et al. (2013) discussed multiple examples where the same trap design performs differently (in terms of swimmer collection) in a variety of settings. Disentangling hydrodynamic effects from zooplankton behavioral influences remains a complex challenge.

Here, we have added a novel swimmer correction technique to the trapper's toolbox, which, uniquely, is available for use *after* traps are retrieved and samples are analyzed. It is not, of course, a substitute for full exclusion of swimmers during trap deployment, or their removal from samples after retrieval, and information about the variation of sample composition with depth and time is lost. A direct validation of this approach awaits future study. However, this method allows retention of information about the overall sinking flux magnitude (here reported as POC flux), and critically, it can reveal the effectiveness of other swimmer exclusion treatments applied during sample collection and processing.

The statistical swimmer correction technique presented here relies on the availability of a handful of samples from the same site and time period, with similar multielement compositions (POC, mass, ^{234}Th activity, bSi, and nonswimmer particle cross-sectional area in gel collectors on the same platform), that together indicate that samples have minimal swimmer contributions. Therefore, we suggest that future studies wishing to explore this correction method utilize sample collection procedures that ensure that a sufficient number of swimmer-free samples are available. We made the assumption that swimmers in a sample would increase carbon but not ^{234}Th or nonswimmer gel area, and we inferred from the patterns in the data that swimmers also added to the mass flux (and *N*, *P*, and PIC) but not to bSi flux. Individual zooplankton were counted for ^{234}Th and found to have very low activities (Buesseler et al., 2020a), but that assumption has not yet been verified directly for bSi. Because the passive flux composition, swimmer composition, and flux profiles will vary from site to site, the application of this correction technique to other studies will also require reevaluation of these assumptions. However, gel particle fluxes and ^{234}Th fluxes will be useful to measure in general because high POC:^{234}Th ratios of swimmer biomass have been reported widely (Buesseler et al., 2006; Passow et al., 2006;

Buesseler et al., 2020a) and because swimmers can be identified easily and excluded from gel trap analyses.

4.1.3. Comparison of measured and predicted ^{234}Th fluxes and implications for trap efficiency

In parallel with the trap sampling conducted here, over 20 spatially distributed profiles of total ^{234}Th were collected during each epoch (Buesseler et al., 2020a). Under steady-state conditions, and in the absence of fluxes carried by vertically migrating zooplankton that bypass sediment traps, fluxes of ^{234}Th computed from the water column deficit of particle-reactive ^{234}Th relative to its conservative parent isotope ^{238}U (termed "predicted ^{234}Th fluxes") should agree with measured fluxes of ^{234}Th into sediment traps (e.g., Buesseler, 1991). However, in several prior studies with high-frequency sampling for ^{234}Th in both the water column and in sediment traps, the difference between predicted ^{234}Th fluxes and trap measurements is positive and typically increases as the total predicted flux increases (Buesseler et al., 2007). In this study, we similarly found measured ^{234}Th fluxes in traps whose mean ($\pm$ standard deviation) values were 33 $\pm$ 19% (n = 32) of the "best estimate" fluxes (mean of steady-state and non-steady-state models; Buesseler et al., 2020a) predicted from water column activities (**Figure 10**). Buesseler et al. (2007) hypothesized that this pattern might be explained by hydrodynamic bias leading to preferential undercollection by traps of the smallest particles that contribute the most to the water column ^{234}Th deficit, or alternatively by episodic, high-flux events that are missed by traps but captured by the longer integration timescale of ^{234}Th measurements. The data collected during EXPORTS include 3D, time-resolved ^{234}Th activities (Buesseler et al., 2020a), simultaneous neutrally buoyant and surface-tethered sediment trap deployments, and measurements of the sinking PSD over particle diameters ranging over three orders of magnitude. Therefore, we have the unique opportunity to evaluate quantitatively the possible drivers of this globally observed pattern.

We first consider timescale because water column-derived ^{234}Th fluxes in this study likely integrated over approximately 20 days preceding sample collection (Buesseler et al., 2020a), while trap samples integrated over 3–6 days. Therefore, one possible explanation of predicted versus measured ^{234}Th flux mismatches could be a high export event preceding the cruise. However, there is no evidence for such an event. Thorium-234 activities stayed relatively constant in Epochs 1 and 2 and increased 6–10% in the upper 60 m by Epoch 3, which leads to a decrease in flux predicted from water column ^{234}Th deficits over the course of the cruise (Buesseler et al., 2020a). Also, no large changes in production indices were observed by autonomous vehicles present prior to the ship arrivals on station in mid-August (Siegel et al., n.d.), nor did fluxes of longer timescale tracers (e.g., ^{210}Pb-^{210}Po) indicate higher export prior to the cruise (Roca-Martí et al., 2020). Horizontal advection of ^{234}Th into surface waters, which cannot be distinguished from a temporal change, possibly could have accounted for some of this increase in ^{234}Th activity by Epoch 3. However, predicted

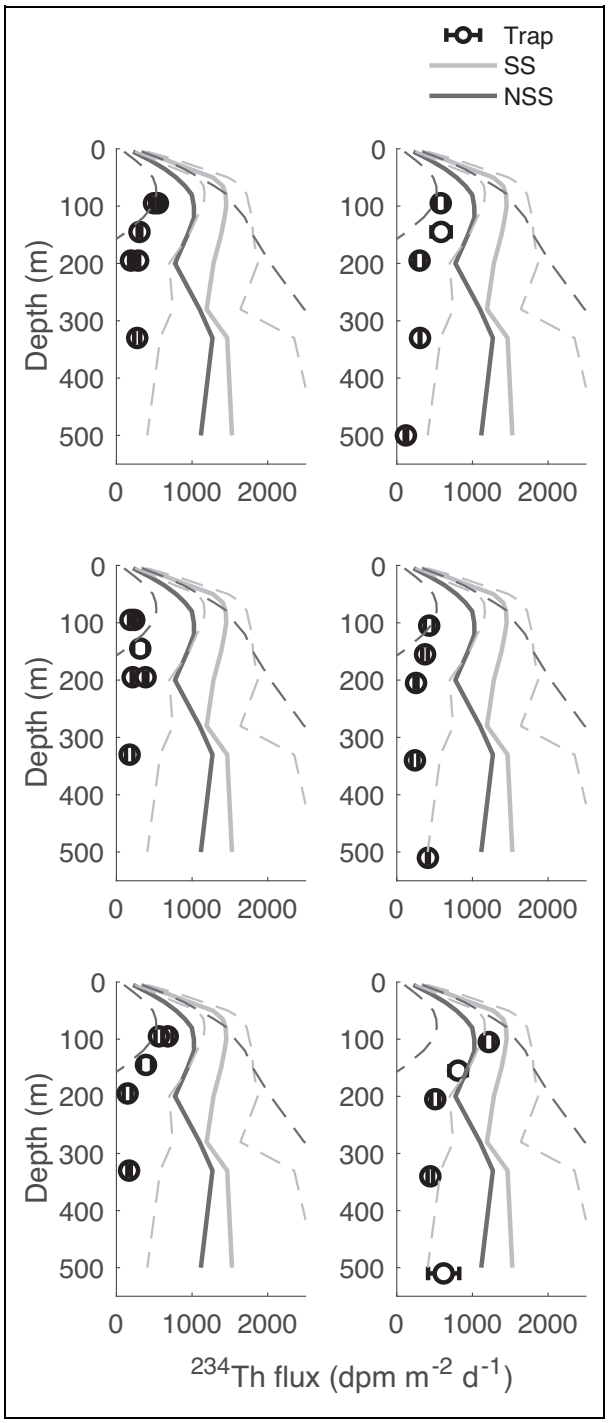

Figure 10. Measured and predicted thorium-234 fluxes. Comparison of measured ^{234}Th fluxes from traps (black circles) and predicted cruise-mean ^{234}Th fluxes from water column deficits according to steady-state (SS; light gray lines; solid and dashed show mean $\pm$ uncertainty) and non-steady-state (NSS; dark gray lines) models. Left panels compare to neutrally buoyant sediment trap fluxes; right panels compare to surface-tethered trap fluxes. Panel row corresponds to epoch. Predicted ^{234}Th fluxes are from Buesseler et al. (2020a). Error bars, which in many cases are smaller than the markers, indicate plus or minus one standard deviation (n = 3) or the range (n = 2) of directly measured splits (see **Table 2**). DOI: https://doi.org/10.1525/elementa.2020.00122.f10

^{234}Th fluxes from a steady-state model (Buesseler et al., 2020a) were unrelated to trap ^{234}Th fluxes (paired t test, $p < 10^{-9}$) regardless of whether spatial averages were computed over the whole ^{234}Th data set or over subsets of measurements specifically within the trap source regions (Figure S5). Overall, these observations suggest that a sampling mismatch over a spatial flux gradient was unlikely to be the main cause of the discrepancy and that export prior to our arrival on station would have made only a minor contribution to the observed mismatch. Below, we discuss comparisons to flux predictions from both the steady-state (SS) and non-steady-state (NSS) models reported by Buesseler et al (2020a), where the latter model is in better agreement with measured fluxes to the traps (**Figure 10**). Each model carries different assumptions about horizontal advection of ^{234}Th and the time variations in the ^{234}Th flux, as described in detail by Buesseler et al. (2020a).

Another possible cause of the discrepancy between water column-derived and measured sediment trap fluxes was that ^{234}Th-bearing particles adhering to the bodies of zooplankton swimmers could have been picked out of the trap samples, inadvertently decreasing the measured trap fluxes (Buesseler et al., 2007). However, in spite of substantial differences in the numbers of swimmers detected in and removed from the different samples (Figure S4), ^{234}Th fluxes were consistent among different trap platforms deployed alongside one another (**Figure 10**; **Table 2**). Furthermore, an independent model predicting carbon flux from images of particles in the gel traps agreed well with the corrected bulk carbon fluxes, as presented by Durkin et al (2021) and discussed above (**Figure 9**; Size distribution of sinking particles section and Statistical Swimmer Correction section).

A number of recent studies have indicated an important role for small (tens of microns and smaller), presumably slowly settling particles in the BCP (Richardson and Jackson 2007; Richardson, 2019). If sediment traps undercollect such particles, then the difference between measured and predicted ^{234}Th fluxes would be expected to grow with an increasing contribution of these small, ^{234}Th-enriched particles to the total flux. We interpret the difference between the modeled and measured fluxes of ^{234}Th carried by 1–32 μm particles (**Figure 11**; Size Distribution of Sinking Particles section) as the flux potentially missed by both the bulk and gel traps due to hydrodynamic effects (Buesseler et al. 2007) or by the gel traps, but not the bulk traps because of microscope resolution limits (Durkin et al., 2015). However, this interpretation of the model rests on the assumption that flattening of the sinking PSD at the small end of the size spectrum (Figure S1) was due to platform or detection effects and not to an actual decrease of the number fluxes of small particles relative to larger ones. While numerous studies support the idea that PSDs of nonsinking particles follow a power-law function at sizes below 32 μm, our ability to confirm this function for sinking particles remains limited at present. Even so, polyacrylamide gel traps and optical microscopy remain the best method for

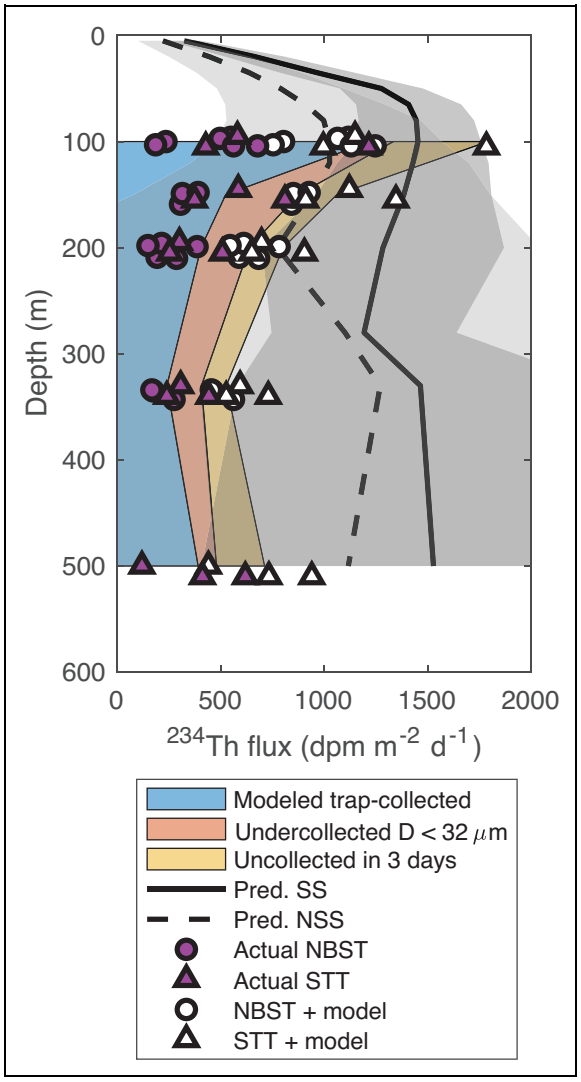

Figure 11. Measured, modeled, and predicted contributions to ^{234}Th flux averaged during the cruise. Filled colored areas illustrate the cumulative contributions to the ^{234}Th flux modeled from extrapolated sinking particle size distributions (see text). These include modeled flux of particles of diameter (D) larger than 32 μm collected by traps (blue, "Modeled trap-collected"), flux carried by smaller, potentially undercollected particles (orange), and flux carried by rare, infrequently collected particles (yellow). Also shown are the predicted ^{234}Th flux from the steady-state (SS) model that assumes flux is constant in time (solid black line and shaded dark gray area showing uncertainty; see text discussion and Buesseler et al., 2020a) and from the non-steady-state (NSS) model that allows for time-varying flux (dashed black line and shaded light gray area; see text discussion and Buesseler et al., 2020a), as well as the measured flux in the neutrally buoyant sediment traps (NBSTs; magenta circles) and surface-tethered traps (STTs; magenta triangles), and the same trap fluxes with added, modeled contributions by small and infrequently collected particles (white symbols). DOI: https://doi.org/10.1525/elementa.2020.00122.f11

quantifying sinking particles with sizes below approximately 100 μm (e.g., Giering et al., 2020). In addition to the reasons given above, another reason to approach this model result with caution is the lack of any systematic difference between NBSTs and STTs in ^{234}Th undercollection (**Figure 10**), even though NBSTs are expected to collect the smallest particles more readily due to their lower hydrodynamic biases (Baker et al., 2020). Finally, the model used a single, mean ^{234}Th:area ratio, which may be inappropriate for particles ranging over orders of magnitude in diameter (e.g., Buesseler et al., 2006).

At the large end of the sinking particle spectrum (diameters roughly 1,000 μm and larger), particles may be less affected by the flow field around traps, given their assumed faster sinking speeds, but they also occur less frequently in low-flux settings such as Station P during the months of our study. The observed mean, size-resolved particle collection rates imply that if a power-law function accurately describes the size distribution of large sinking particles, then particles larger than about 2,000–3,000 μm had <5% probability of being collected during a 3-day deployment (Figure S2), even though modeled fluxes of those particles accounted for up to 9% of the total (**Figure 11**). The simple model of "undercollected, rare-particle flux" that is presented here is conservative in its calculation of the probability of collecting five particles in 3 days. Both increasing the deployment length and decreasing the required number of particles would decrease the magnitude of the modeled undercollection. Any departure of the true, sinking PSD from the power-law model (Equation 1) at the large end of the spectrum would also add uncertainty to the modeled, undercounted flux from large particles. Unfortunately, the size distributions of large, sinking particles are not well constrained in general. The probability of collecting rare, large particles will increase, however, as the collection rates of these particles increase in higher flux settings. Therefore, undercounting is likely to be most problematic in low-flux settings with only occasional, outsized contributions of rare, large particles. Observations of salp patches, and occasional collection of salp fecal pellets that dominated modeled carbon flux to traps, suggest that such undercounting may have been the case during our study (Steinberg et al., 2020; Durkin et al., 2021).

The simple assumptions made in our model of ^{234}Th fluxes carried by different particle classes allow us to coarsely evaluate the possible contribution of trap collection biases to the mismatch between trap and water column ^{234}Th fluxes. Addition of the mean, modeled small-particle and rare-particle fluxes to the trap observations could plausibly close the gap between trap and predicted ^{234}Th fluxes from the non-steady-state model at depths between 100 and 200 m (**Figure 11**). However, this approach did not work with respect to the steady-state model flux predictions or at depths below 200 m, where a gap of several hundred dpm m^{-2} d^{-1} remained (**Figure 11**).

In parallel with possible trap inefficiencies, fluxes carried by zooplankton vertical migrants could also be reflected in the water column ^{234}Th deficits but not collected by the traps. Actively migrating zooplankton feed near the surface and then release ^{234}Th at depth through respiration or excretion of the associated carbon, bypassing traps but contributing to the water column deficit (Longhurst et al., 1990; Steinberg et al., 2000; Steinberg and Landry, 2017). We next assess whether the magnitude of the observed trap-water column mismatch is consistent with an independent estimate of the carbon dioxide and DOC fluxes carried below 100 m by diel vertical migrators, which together averaged 0.4 mmol C m^{-2} d^{-1} (A Maas, personal communication).

The cruise-average, trap-water column ^{234}Th flux mismatch at 100 m was 428 dpm m^{-2} d^{-1} (non-steady-state model) or 854 dpm m^{-2} d^{-1} (steady-state model). The conversion to carbon flux depends on the POC:^{234}Th ratio (for brevity, C:Th ratio) of particles consumed by migrating zooplankton. In the mixed layer, particles smaller than 5 μm in diameter had a C:Th ratio of 3.95 μmol dpm^{-1}, while larger 5–51 μm particles at 100 m had a C:Th ratio of 1.62 μmol dpm^{-1} (Buesseler et al., 2020a). These choices represent the high and low end of likely C:Th ratios. Depending on which flux model and C:Th ratio are chosen, the corresponding POC flux would range from 0.7 to 3.4 mmol C m^{-2} d^{-1}. Therefore, only in the scenario where the non-steady-state model is used to predict ^{234}Th flux, and a relatively low C:Th ratio is assumed, is the active flux by itself (0.4 mmol C m^{-2} d^{-1}) of similar magnitude to the trap-water column ^{234}Th flux mismatch. This comparison obviously rests upon a number of assumptions about the depth structure of zooplankton migration, the nature of food particles consumed, and the degree of actual undercollection and undercounting of particles by sediment traps. A more detailed exploration of these assumptions awaits further work, but this initial estimate suggests that part of the trap-water column ^{234}Th flux mismatch could plausibly be due to active transport of carbon by vertical migrants, especially at the upper trap depths where their contribution should be the largest. However, this process does not address the larger trap-water column mismatch observed at deeper depths.

4.2. Characterizing the BCP during the EXPORTS North Pacific cruise

The overarching EXPORTS program goal is to characterize the BCP and related satellite observables across a range of ecosystem states, so that predictive, mechanistic models generalizable to the global ocean can be developed. To that end, the comparison of BCP strength and efficiency as measured here to other estimates will help to contextualize the North Pacific field campaign, which was meant to serve as one end-member of a broader comparison (Siegel et al., n.d.). Buesseler and Boyd (2009), and more recently Buesseler et al. (2020b), proposed the use of two metrics, the export ratio at the euphotic zone depth (Ez-ratio) and the 100-m transfer efficiency (T_{100}), to describe and compare the BCP across regions and seasons.

The cruise-mean Ez-ratio observed here (0.10 ± 0.06) was consistent with an earlier measurement of 0.13 at Station P in August (Charette et al., 1999; Buesseler and Boyd, 2009). Our measured transfer efficiency (0.55 ±

0.35) is higher than the Charette et al. (1999) estimate of $T_{100} = 0.3$, although in that study T_{100} was assessed at 40 m, which was likely well within the euphotic zone, resulting in a lower T_{100} value (Buesseler et al., 2020a). Here, we have assessed the Ez-ratio and T_{100} metrics at a depth slightly above the 0.1% light level. The difference between the upper trap depth (95–105 m) and z_{eu} (112 $\pm$ 7 m, $n =$ 11) is small, and interpolating the trap fluxes to 112 m would have introduced additional uncertainty. Parallel, independent estimates of the Ez-ratio and T_{100} parameters were made using carbon flux predicted from ^{234}Th deficits and C:^{234}Th ratios in large-volume pump samples (Buesseler et al., 2020a). For the "best estimate" of ^{234}Th flux in that study, computed as the mean of the steady-state and non-steady-state models with an assumed euphotic zone depth of 120 m, the ^{234}Th-based Ez-ratio was 0.13 ($\pm$ 0.05; uncertainty from NPP and numerous ^{234}Th flux measurements during cruise; see Buesseler et al., 2020a for details). The ^{234}Th-based T_{100} estimate computed between 120 m and 220 m was 0.61 ($\pm$ 0.46). At the shallower, 100-m reference depth used in this study, T_{100} estimated from the water column data would have decreased to 0.53 ($\pm$ 0.39) because of the rapid flux attenuation observed around the base of the euphotic zone (Buesseler et al., 2020a). Overall, Ez-ratios and T_{100} values determined from the two studies were in good agreement (**Figure 7**).

A detailed discussion of literature reports of BCP strength and efficiency at Station P is presented in Buesseler et al. (2020a). Briefly, prior work with both sediment traps and ^{234}Th measurements indicates that the August–September period at Station P is one of generally low and declining export fluxes compared to earlier in the season (Timothy et al., 2013). Our observations are consistent with this finding. The shifts we observed in BCP strength and efficiency on weekly timescales are striking in comparison to the global range of similar measurements (**Figure 7**; see also a summary of global data in Buesseler and Boyd, 2009, updated in Buesseler et al., 2020b). For instance, our trap observations show that the first two sampling epochs had high and variable transfer efficiencies (0.6–0.9; **Table 3**) and low, relatively well-constrained Ez-ratios (0.06–0.08), which makes them more similar to subtropical, oligotrophic sites like HOT and BATS (Buesseler and Boyd, 2009). In contrast, the third sampling epoch saw an increase in both the magnitude and variability of the Ez-ratio (to 0.18 $\pm$ 0.06), coupled with a decrease in T_{100} to 0.4 ($\pm$ 0.2), which is more consistent with earlier observations at Station P in late summer (Charette et al., 1999). Shifts in proxies for biological stocks and rates, from Epochs 1 and 2 to Epoch 3, included increases in surface POC, phytoplankton pigments, and bSi concentrations (Siegel et al., n.d.). Forthcoming, more detailed investigations of the underlying biological processes and surface community composition will allow us to better contextualize these observed, temporal shifts in fluxes to the traps.

In spite of the larger week-to-week changes in Ez-ratio and T_{100} measurements, their product, which gives the overall efficiency with which NPP is transferred to 100 m below the reference depth, was well constrained across sampling epochs (0.055 $\pm$ 0.010, $n = 3$). Compensation for an increase in the export efficiency with a decrease in the transfer efficiency during the course of the cruise is consistent with tight coupling between production and recycling in the ecosystem in the northeast, subarctic Pacific Ocean (Wassman et al., 1998; Buesseler and Boyd, 2009). Also suggestive of this coupling were the types of particles observed in gel traps and Marine Snow Catchers deployed during EXPORTS. Phytoplankton aggregates and cells made only minimal contributions to the sinking flux, which appeared to be heavily modulated by grazers (McNair and Menden-Deuer, 2020; Durkin et al., 2021; U Passow, personal communciation). Future investigations will examine possible connections of these observations to biological rates and the ecosystem structure measured during EXPORTS.

5. Conclusion

We have presented the initial results from the EXPORTS North Pacific sediment trap sampling program, discussed the general patterns that were observed, and analyzed the major sources of uncertainty in our findings. This work includes the development of a novel method to correct for swimmer carbon in the sediment traps and the use of detailed measurements of sinking PSD to estimate ^{234}Th fluxes via undercollected small particles and undercounted rare, large particles and to constrain potential ^{234}Th fluxes due to active zooplankton transport. Future studies will examine more closely the role of active transport in carrying POC fluxes to depth; the spatiotemporal changes in physical drivers and ecosystem structure that might be responsible for changes in BCP efficiency on weekly timescales; and the detailed biological identities, fluxes, and attenuation with depth of sinking particles collected in gel traps (Durkin et al., 2021).

Data accessibility statement

The data presented here are available at the NASA SeaBASS and R2R repositories, with the following references:

Sediment trap trajectories and bulk flux data:

Estapa, ML, EXPORTS. SeaWiFS Bio-optical Archive and Storage System (SeaBASS). NASA. Available at https://seabass.gsfc.nasa.gov. Accessed 28 May 2020.

Gel trap imagery and particle size distributions:

Durkin, CA, EXPORTS. SeaWiFS Bio-optical Archive and Storage System (SeaBASS). NASA. Available at https://seabass.gsfc.nasa.gov. Accessed 28 May 2020.

^{234}Th data:

Buesseler, KO, EXPORTS. SeaWiFS Bio-optical Archive and Storage System (SeaBASS). NASA. Available at https://seabass.gsfc.nasa.gov. Accessed 28 May 2020.

Net primary production data:

Behrenfeld, M, EXPORTS. SeaWiFS Bio-optical Archive and Storage System (SeaBASS). NASA. Available at https://seabass.gsfc.nasa.gov. Accessed 28 May 2020.

Lagrangian float chlorophyll profiles:

D'Asaro, E, EXPORTS. SeaWiFS Bio-optical Archive and Storage System (SeaBASS). NASA. Available at https://seabass.gsfc.nasa.gov. Accessed 28 May 2020.

Ship ADCP velocities:

Roger Revelle RR1813 Cruise Data. Rolling Deck to Repository. UNOLS. Available at https://www.rvdata.us/search/cruise/RR1813. Accessed 26 June 2020. http://dx.doi.org/10.7284/908060.

Sally Ride SR1812 Cruise Data. Rolling Deck to Repository. UNOLS. Available at https://www.rvdata.us/search/cruise/SR1812. Accessed 26 June 2020. http://dx.doi.org/10.7284/908060.

Photosynthetically available radiation (PAR) data:

Siegel, DA, EXPORTS. SeaWiFS Bio-optical Archive and Storage System (SeaBASS). NASA. Available at https://seabass.gsfc.nasa.gov. Accessed 28 May 2020.

Supplemental files

The supplemental files for this article can be found as follows:

Text S1. Matlab code to carry out the swimmer correction procedure outlined in the main text and illustrated in **Figure 4**.

Figure S1. Composite figure showing particle size distribution spectra from all gel trap samples and fit of a power-law function to the data.

Figure S2. Figure showing the probability of collecting $\geq$5 particles during a trap deployment, as a function of particle size (1 μm to 1 cm) and depth (100–500 m).

Figure S3. Relative horizontal current speeds at the bottom of the surface-tethered trap array.

Figure S4. Profiles of proxies for swimmer intrusion into sediment traps.

Figure S5. Modeled particle source funnels for each trap, for particles sinking 100 m d^{-1}.

Acknowledgments

The deployments and laboratory analyses reported here would have been impossible without the guidance and assistance of many people. The EXPORTS program has benefited from the leadership of the scientists in the EXPORTS project office. Maureen Auro, Annie Bodel, Sam Clevenger, Jessica Drysdale, Melanie Feen, Tristan Horner, Jen Kenyon, Jackson Sugar, and Kaitlyn Tradd all helped with laboratory and equipment preparation. The authors also thank the captains and crews of the *R/V Roger Revelle* and *R/V Sally Ride* and our fellow scientists and shipmates who provided invaluable assistance and support at sea. Finally, they appreciate the willingness of Amy Maas, James Fox, Hilary Close, Abigale Wyatt, and Laure Resplandy to share their preliminary observations of active transport, net primary production, stable isotope compositions of trap samples, and water column ^{234}Th flux predictions in support of this study.

Funding

The authors would like to acknowledge funding support from the NASA EXPORTS program (Award 80NSSC17K0662) for all sediment trap data presented here. Net primary production data collection was supported by EXPORTS (Award 80NSSC17K568) to Oregon State University. Thorium data collection was supported by EXPORTS (Award 80NSSC17K0555) to KB, CRBN, and L. Resplandy.

Competing interests

The authors declare that they have no conflict of interest.

Author contributions

Substantial contributions to conception and design: ME, KB, CAD, MO.

Acquisition of data: ME, KB, CAD, MO, CRBN, EB, RPK, SP, MRM.

Analysis and interpretation of data: ME, KB, CAD, MO, CRBN, EB, RPK, SP, MRM.

Drafting the article or revising it critically for important intellectual content: LE, KB, CAD, MO, CRBN, EB, RPK, SP, MRM.

Final approval of the version to be published: ME, KB, CAD, MO, CRBN, EB, RPK, SP, MRM.

References

Amaral, VJ, Marchal, O, Lee, J-M, Lam, PJ, Roca-Martí, M, Buesseler, K. 2020 February. Estimation of particle (dis)aggregation rates from the joint inversion of POC, Al, and Ti concentration data. Ocean Sciences Meeting; San Diego, CA.

Baker, CA, Estapa, ML, Iversen, M, Lampitt, R, Buesseler, K. 2020. Are all sediment traps created equal? An intercomparison study of carbon export methodologies at the PAP-SO site. *Progress in Oceanography* **184**: 102317. DOI: http://dx.doi.org/10.1016/j.pocean.2020.102317.

Boyd, PW, Claustre, H, Levy, M, Siegel, DA, Weber, T. 2019. Multi-faceted particle pumps drive carbon sequestration in the ocean. *Nature* **568**(7752): 327–335. DOI: http://dx.doi.org/10.1038/s41586-019-1098-2.

Brzezinski, MA, Nelson, DM. 1989. Seasonal changes in the silicon cycle within a Gulf Stream warm-core ring. *Deep Sea Research Part A: Oceanographic Research Papers* **36**(7): 1009.

Buesseler, KO. 1991. Do upper-ocean sediment traps provide an accurate record of particle flux? *Nature* **353**(6343): 420–423. DOI: http://dx.doi.org/10.1038/353420a0.

Buesseler, KO, Antia, AN, Chen, M, Fowler, SW, Gardner, WD, Gustafsson, O, Harada, K, Michaels, AF, Rutgers van der Loeff, M, Sarin, M, Steinberg, DK. 2007. An assessment of the use of sediment traps for estimating upper ocean particle fluxes. *Journal of Marine Research* **65**(3): 345–416. DOI: http://dx.doi.org/10.1357/002224007781567621.

Buesseler, KO, Benitez-Nelson, CR, Moran, SB, Burd, A, Charette, M, Cochran, JK, Coppola, L, Fisher, NS, Fowler, SW, Gardner, WD, Guo, LD. 2006. An assessment of particulate organic carbon to thorium-234 ratios in the ocean and their impact on the application of ^{234}Th as a POC flux proxy. *Marine Chemistry* **100**: 213–233. DOI: http://dx.doi.org/10.1016/j.marchem.2005.10.013.

Buesseler, KO, Benitez-Nelson, CR, Roca-Marti, M, Wyatt, AM, Resplandy, L, Clevenger, SJ, Drysdale, J, Estapa, ML, Pike, S, Umhau, BP. 2020a. High resolution spatial and temporal measurements

of particulate organic carbon flux using thorium-234 in the NE Pacific Ocean during the EXPORTS Program. *Elementa: Science of the Anthropocene* **8**(1): 030.

Buesseler, KO, Boyd, PW. 2009. Shedding light on processes that control particle export and flux attenuation in the twilight zone of the open ocean. *Limnology and Oceanography* **54**(4): 1210–1232.

Buesseler, KO, Boyd, PW, Black, EE, Siegel, DA. 2020b. Metrics that matter for assessing the ocean biological carbon pump. *Proceedings of the National Academy of Sciences* **117**(18): 9679–9687. DOI: http://dx.doi.org/10.1073/pnas.1918114117.

Charette, MA, Moran, SB, Bishop, JKB. 1999. ^{234}Th as a tracer of particulate organic carbon export in the subarctic northeast Pacific Ocean. *Deep Sea Research Part II: Topical Studies in Oceanography* **46**(11): 2833–2861. DOI: http://dx.doi.org/10.1016/S0967-0645(99)00085-5.

Close, HG, Wojtal, PK, Henderson, LC, Benitez-Nelson, CR, Buesseler, KO, Estapa, ML, Pike, SM, Popp, BN, Roca-Martí, M. 2020 February. Estimating relative flux of phytodetritus, fecal pellets, and bacterial biomass using compound-specific isotope analysis of amino acids at Station Papa (EXPORTS). Ocean Sciences Meeting; San Diego, CA.

Coale, KH. 1990. Labyrinth of doom: A device to minimize the "swimmer" component in sediment trap collections. *Limnology and Oceanography* **35**(6): 1376–1381. DOI: http://dx.doi.org/10.4319/lo.1990.35.6.1376.

Durkin, CA, Buesseler, KO, Cetinić, I, Estapa, ML, Kelly, RP, Omand, M. 2021 Jan 1. A visual tour of carbon export by sinking particles. DOI: http://dx.doi.org/10.1101/2021.02.16.431317.

Durkin, CA, Estapa, ML, Buesseler, KO. 2015. Observations of carbon export by small sinking particles in the upper mesopelagic. *Marine Chemistry* **175**: 72–81. DOI: http://dx.doi.org/10.1016/j.marchem.2015.02.011.

Estapa, M, Valdes, J, Tradd, K, Sugar, J, Omand, M, Buesseler, K. 2020. The neutrally buoyant sediment trap: Two decades of progress. *Journal of Atmospheric and Oceanic Technology* **37**(6): 957–973. DOI: http://dx.doi.org/10.1175/JTECH-D-19-0118.1.

Estapa, ML. EXPORTS. 2019**.** SeaWiFS Bio-optical Archive and Storage System (SeaBASS), NASA. Available at https://seabass.gsfc.nasa.gov. Accessed 28 May 2020.

Estapa, ML, Durkin, C, Buesseler, K, Johnson, R, Feen, M. 2017. Carbon flux from bio-optical profiling floats: Calibrating transmissometers for use as optical sediment traps. *Deep Sea Research Part I: Oceanographic Research Papers* **120**: 100–111. DOI: http://dx.doi.org/10.1016/j.dsr.2016.12.003.

Fox, J, Behrenfeld, MJ, Haentjens, N, Chase, A, Kramer, SJ, Boss, E, Karp-Boss, L, Fisher, NL, Penta, WB, Westberry, TK, Halsey, KH. 2020. Phytoplankton growth and productivity in the western North Atlantic: Observations of regional variability from the NAAMES field campaigns. *Frontiers in Marine Science* **7**: 24. DOI: http://dx.doi.org/10.3389/fmars.2020.00024.

Gardner, WD. 1977. Fluxes, dynamics and chemistry of particulates in the ocean [Ph.D.]. Cambridge, MA: MIT/WHOI Joint Program in Oceanography.

Giering, SLC, Cavan, EL, Basedow, SL, Briggs, N, Burd, AB, Darroch, LJ, Guidi, L, Irisson, J-O, Iversen, MH, Kiko, R, Lindsay, D. 2020. Sinking organic particles in the ocean—Flux estimates from in situ optical devices. *Frontiers in Marine Science* **6**: 834. DOI: http://dx.doi.org/10.3389/fmars.2019.00834.

Guidi, L, Stemmann, L, Jackson, GA, Ibanez, F, Claustre, H, Legendre, L, Picheral, M, Gorskya, G. 2009. Effects of phytoplankton community on production, size, and export of large aggregates: A world-ocean analysis. *Limnology and Oceanography* **54**(6): 1951–1963. DOI: http://dx.doi.org/10.4319/lo.2009.54.6.1951.

Hedges, JI, Baldock, JA, Gelinas, Y, Lee, C, Peterson, ML, Wakeham, SG. 2002. The biochemical and elemental compositions of marine plankton: A NMR perspective. *Marine Chemistry* **78**(1): 47–63.

Honjo, S, Francois, R, Manganini, S, Dymond, J, Collier, R. 2000. Particle fluxes to the interior of the Southern Ocean in the Western Pacific sector along 170.3W. *Deep Sea Research Part II: Topical Studies in Oceanography* **47**: 3521–3548.

Karl, DM, Winn, CD, Hebel, DVW, Letelier, R. 1990. *Hawaii Ocean Time-Series Program field and laboratory protocols*. Honolulu, Hawaii: University of Hawaii Press.

Kawakami, H, Honda, MC, Matsumoto, K, Fujiki, T, Watanabe, S. 2010. East-west distribution of POC fluxes estimated from 234Th in the northern North Pacific in autumn. *Journal of Oceanography* **66**(1): 71–83. DOI: http://dx.doi.org/10.1007/s10872-010-0006-z

Knap, AH, Michaels, AF, Steinberg, DK, Bahr, F, Bates, NR, Bell, S, Countway, P, Close, A, Doyle, A, Howse, F, Gundersen, K, Johnson, RJ, Kelly, R, Little, R, Orcutt, K, Parsons, R, Rathburn, C, Sanderson, M, Stone, S. 1997. *BATS methods manual*. Woods Hole, MA: U.S. JGOFS Planning Office.

Knauer, GA, Martin, JH, Bruland, KW. 1979. Fluxes of particulate carbon, nitrogen, and phosphorus in the upper water column of the northeast Pacific. *Deep Sea Research Part A: Oceanographic Research Papers* **26**(1): 97–108.

Lamborg, CH, Buesseler, KO, Lam, PJ. 2008. Sinking fluxes of minor and trace elements in the North Pacific Ocean measured during the VERTIGO program. *Deep Sea Research Part II: Topical Studies in Oceanography* **55**(14): 1564–1577. DOI: http://dx.doi.org/10.1016/j.dsr2.2008.04.012.

Laurenceau-Cornec, EC, Moigne, FACL, Gallinari, M, Moriceau B, Toullec, J, Iversen, MH, Engel, A, Rocha, CLDL. 2019. New guidelines for the application of Stokes' models to the sinking velocity of marine aggregates. *Limnology and Oceanography*

64: 1264–1285. DOI: http://dx.doi.org/10.1002/lno.11388.

Lee, C, Wakeham, SG, Hedges, JI. 1988. The measurement of oceanic particle flux—Are "swimmers" a problem? *Oceanography* **11**: 34–36.

Levy, M, Bopp, L, Karleskind, P, Resplandy, L, Ethe, C, Pinsard, F. 2013. Physical pathways for carbon transfers between the surface mixed layer and the ocean interior. *Global Biogeochemical Cycles* **27**(4): 1001–1012. DOI: http://dx.doi.org/10.1002/gbc.20092.

Longhurst, AR, Bedo, AW, Harrison, WG, Head, EJH, Sameoto, DD. 1990. Vertical flux of respiratory carbon by oceanic diel migrant biota. *Deep Sea Research Part A: Oceanographic Research Papers* **37**(4): 685–694. DOI: http://dx.doi.org/10.1016/0198-0149(90)90098-G.

Mackinson, BL, Moran, SB, Lomas, MW, Stewart, GM, Kelly, RP. 2015. Estimates of micro-, nano-, and picoplankton contributions to particle export in the northeast Pacific. *Biogeosciences* **12**(11): 3429–3446. DOI: http://dx.doi.org/10.5194/bg-12-3429-2015.

Malmstrom, R. 2015. RNAlater Recipe v1. DOI: http://dx.doi.org/10.17504/protocols.io.c56y9d.

Marra, JF, Lance, VP, Vaillancourt, RD, Hargreaves, BR. 2014. Resolving the ocean's euphotic zone. *Deep Sea Research Part I: Oceanographic Research Papers* **83**: 45–50. DOI: http://dx.doi.org/10.1016/j.dsr.2013.09.005.

McCave, IN. 1984. Size spectra and aggregation of suspended particles in the deep ocean. *Deep Sea Research Part A: Oceanographic Research Papers* **31**(4): 329–352. DOI: http://dx.doi.org/10.1016/0198-0149(84)90088-8.

McKinley, GA, Fay, AR, Lovenduski, NS, Pilcher, DJ. 2017. Natural variability and anthropogenic trends in the ocean carbon sink. *Annual Review of Marine Science* **9**(1): 125–150. DOI: http://dx.doi.org/10.1146/annurev-marine-010816-060529.

McNair, H, Menden-Deuer, S. 2020. Protist grazing contributes to microbial food web at the upper boundary of the twilight zone in the subarctic Pacific. *Marine Ecology Progress Series* **636**: 235–241. DOI: http://dx.doi.org/10.3354/meps13246.

Michaels, AF, Silver, MW, Gowing, MM, Knauer, GA. 1990. Cryptic zooplankton "swimmers" in upper ocean sediment traps. *Deep Sea Research Part A: Oceanographic Research Papers* **37**(8): 1285–1296. DOI: http://dx.doi.org/10.1016/0198-0149(90)90043-U.

Owens, SA, Buesseler, KO, Lamborg, CH, Valdes, J, Lomas, MW, Johnson, RJ, Steinberg, DK, Siegel, DA. 2013. A new time series of particle export from neutrally buoyant sediments traps at the Bermuda Atlantic Time-Series Study site. *Deep Sea Research Part I: Oceanographic Research Papers* **72**: 34–47. DOI: http://dx.doi.org/10.1016/j.dsr.2012.10.011.

Owens, SA, Pike, S, Buesseler, KO. 2015. Thorium-234 as a tracer of particle dynamics and upper ocean export in the Atlantic Ocean. *Deep Sea Research Part II: Topical Studies in Oceanography* **116**: 42–59. DOI: http://dx.doi.org/10.1016/j.dsr2.2014.11.010.

Palevsky, HI, Doney, SC. 2018. How choice of depth horizon influences the estimated spatial patterns and global magnitude of ocean carbon export flux. *Geophysical Research Letters* **45**(9): 4171–4179. DOI: http://dx.doi.org/10.1029/2017GL076498.

Passow, U, Dunne, J, Murray, JW, Balistrieri, L, Alldredge, AL. 2006. Organic carbon to ^{234}Th ratios of marine organic matter. *Marine Chemistry* **100**(3–4): 323–336. DOI: http://dx.doi.org/10.1016/j.marchem.2005.10.020.

Peterson, ML, Wakeham, SG, Lee, C, Askea, MA, Miquel, JC. 2005. Novel techniques for collection of sinking particles in the ocean and determining their settling rates: Sinking particle collection techniques. *Limnology and Oceanography: Methods* **3**(12): 520–532. DOI: http://dx.doi.org/10.4319/lom.2005.3.520.

Press, WH, Teukolsky, SA, Vetterling, WT, Flannery, BP. 2007. *Numerical recipes: The art of scientific computing*. Third edition. Cambridge University Press.

Richardson, TL. 2019. Mechanisms and pathways of small-phytoplankton export from the surface ocean. *Annual Review of Marine Science* **11**(1): 57–74. DOI: http://dx.doi.org/10.1146/annurev-marine-121916-063627.

Richardson, TL, Jackson, GA. 2007. Small phytoplankton and carbon export from the surface ocean. *Science* **315**(5813): 838–840. DOI: http://dx.doi.org/10.1126/science.1133471.

Roca-Martí, M, Estapa, ML, Masque, P, Benitez-Nelson, CR, Buesseler, KO. 2020 February. Polonium-210 and Lead-210 as tracers of particle export and attenuation on the first EXPORTS cruise at Station PAPA. Ocean Sciences Meeting; San Diego, CA.

Romanelli, E, Giering, SLC, Siegel, DA, Passow, U. 2020 February. Assessment of sinking particle size spectra from Marine Snow Catcher deployments during EXPORTS. Ocean Sciences Meeting; San Diego, CA.

Santoro, A, Albers, J, Durkin, CA, Bressac, M, Estapa, ML, Buesseler, KO, Omand, MM, Passow, U, Boyd, PW. 2020 February. Microbial community composition on sinking particles as a function of depth and particle type in the North Pacific. Ocean Sciences Meeting; San Diego, CA.

Sheldon, RW, Prakash, A, Sutcliffe Jr WH. 1972. The size distribution of particles in the ocean. *Limnology and Oceanography* **17**(3): 327–340.

Siegel, DA, Buesseler, KO, Behrenfeld, MJ, Benitez-Nelson, CR, Boss, E, Brzezinski, MA, Burd, A, Carlson, CA, D'Asaro, EA, Doney, SC, Perry, MJ. 2016. Prediction of the export and fate of global ocean net primary production: The EXPORTS science plan. *Frontiers in Marine Science* **3**. DOI: http://dx.doi.org/10.3389/fmars.2016.00022.

Siegel, DA, Cetinic, I, Graff, J, Lee, C, Nelson, N, Perry, MJ, Soto Ramos, I, Steinberg, D, Buesseler, K, Fassbender, A, et al. n.d. Overview of the Export Processes in the Ocean from RemoTe Sensing (EXPORTS) Northeast Pacific field deployment. *Elementa: Science of the Anthropocene*, in press.

Siegel, DA, Deuser, WG. 1997. Trajectories of sinking particles in the Sargasso Sea: Modeling of statistical funnels above deep-ocean sediment traps. *Deep Sea Research Part I: Oceanographic Research Papers* **44**(9): 1519–1541.

Siegel, DA, Fields, E, Buesseler, KO. 2008. A bottom-up view of the biological pump: Modeling source funnels above ocean sediment traps. *Deep Sea Research Part I: Oceanographic Research Papers* **55**(1): 108–127.

Steinberg, DK, Carlson, CA, Bates, NR, Goldthwait, SA, Madin, LP, Michaels, AF. 2000. Zooplankton vertical migration and the active transport of dissolved organic and inorganic carbon in the Sargasso Sea. *Deep Sea Research Part I: Oceanographic Research Papers* **47**(1): 137–158.

Steinberg, DK, Landry, MR. 2017. Zooplankton and the ocean carbon cycle. *Annual Review of Marine Science* **9**(1): 413–444. DOI: http://dx.doi.org/10.1146/annurev-marine-010814-015924.

Steinberg, DK, Stamieszkin, K, Maas, AE, Durkin, CA, Passow, U, Estapa, ML, Buesseler, KO, Roca-Martí, M, Omand, MM. 2020 February. Salp-mediated export processes in the northeast subarctic Pacific Ocean. Ocean Sciences Meeting; San Diego, CA.

Timothy, DA, Wong, CS, Barwell-Clarke, JE, Page, JS, White, LA, Macdonald, RW. 2013. Climatology of sediment flux and composition in the subarctic Northeast Pacific Ocean with biogeochemical implications. *Progress in Oceanography* **116**: 95–129. DOI: http://dx.doi.org/10.1016/j.pocean.2013.06.017.

Wassmann, P. 1998. Retention versus export food chains: Processes controlling sinking loss from marine pelagic systems. *Hydrobiologia* **363**(1): 29–57. DOI: http://dx.doi.org/10.1023/A:1003113403096.

How to cite this article: Estapa, M, Buesseler, K, Durkin, CA, Omand, M, Benitez-Nelson, CR, Roca-Martí, M, Breves, E, Kelly, RP, Pike, S. 2021. Biogenic sinking particle fluxes and sediment trap collection efficiency at Ocean Station Papa. *Elementa: Science of Anthropocene* 9(1). DOI: https://doi.org/10.1525/elementa.2020.00122.

Domain Editor-in-Chief: Jody W. Deming, University of Washington, Seattle, WA, USA

Associate Editor: Laurenz Thomsen, Department of Earth and Space Sciences, Jacobs University Bremen, Bremen, Germany

Knowledge Domain: Ocean Science

Part of an Elementa Special Feature: Accomplishments from the EXport Processes in the Ocean from RemoTe Sensing (EXPORTS) Field Campaign to the Northeast Pacific Ocean

Published: June 17, 2021 **Accepted:** March 28, 2021 **Submitted:** August 20, 2020

ELEMENTA Science of the Anthropocene

Elem Sci Anth is a peer-reviewed open access journal published by University of California Press.

OPEN ACCESS